Astronomy & Astrophysics manuscript no. output
November 12, 2026
©ESO 2026

Euclid Data Release 1 (DR1)

The *Euclid* surveys at DR1

Euclid Collaboration: I. Tereno, J. Dinis, X. Dupac, R. Scaramella, B. Altieri, H. Aussel, I. Baldry, P. Battaglia, et al.

(Full author list and affiliations details can be found after the references)

November 12, 2026

ABSTRACT

Euclid is a surveying mission that is progressively imaging and spectroscopically mapping a wide area of extragalactic sky in visible and near infrared bands. The *Euclid* mission is, however, not restricted to the Euclid Wide Survey, but it includes data from various other survey components. This paper presents the Data Release 1 (DR1) status of the multiple *Euclid* surveys and fields, including the Euclid Deep Survey, Euclid Auxiliary Fields, calibration fields, the Euclid Medium-Deep Survey, the Euclid Ecliptic Survey, and the Independent Legacy Scientists' field, in addition to the Euclid Wide Survey. Some of these fields were observed during the initial Performance-Verification phase, others during the Phase-Diversity calibration campaign, and the majority during the subsequent science operations phase. This paper describes the different procedures of survey implementation applied in the various phases of the mission, from the set of requirements, constraints, and limitations, to the final operational products used to operate the spacecraft and execute the science surveys. The resulting main component of the *Euclid* surveys, the Euclid Wide Survey, covers at DR1 an area of 2100 deg^2, in two separate regions, of which 1900 deg^2 corresponds to data validated in higher-level processing.

Key words. Surveys – Space vehicles – Methods: numerical – Cosmology: observations

1. Introduction

Euclid (Euclid Collaboration: Mellier et al. 2025) is a survey mission. One of its fundamental requirements is to carry out the Euclid Wide Survey (EWS) to conduct its two primary scientific experiments, galaxy clustering and weak gravitational lensing, covering at least 14 000 deg^2 of the extragalactic sky. EWS observations started on 14 February 2024 and will continue until the nominal end of the mission on 31 December 2029. At the same time, *Euclid* also performs the Euclid Deep Survey (EDS), consisting of repeated observations of the three Euclid Deep Fields (EDFs), namely the North (EDF-N), South (EDF-S) and Fornax (EDF-F) fields. The EDS will accumulate greater depth than that of the EWS, up to a gain of about 2 magnitudes. It also observes six so-called auxiliary fields, supporting instrument calibration and characterising the source population, and acquires data on specific fields at specific cadences to perform calibration activities necessary to process and analyse the EWS data. The observations of these four components of the *Euclid* survey, namely the EWS, the EDS, the Euclid Auxiliary Fields (EAFs), and calibrations, are scheduled in a time-ordered sequence of pointings and spacecraft slews, known as a reference survey definition (RSD).

The *Euclid* survey is however not restricted to the RSD components. During the period of 7.5 months between launch on 1 July 2023 and the start of the RSD execution, other observations were made over 3 phases, namely the spacecraft commissioning, the performance-verification (PV) phase, and the phase-diversity calibration (PDC) campaign. The commissioning of the *Euclid* spacecraft was completed on 4 August 2023. It was followed by the PV phase (Euclid Collaboration: Schirmer et al. 2026a) that lasted until the beginning of December 2023, longer than originally planned to include investigation, testing, and validation activities associated with spacecraft anomalies detected during commissioning (Laureijs et al. 2024). The PDC campaign, started on 3 December 2023, is a first component of the strategy to build and calibrate a point-spread function (PSF) model (Euclid Collaboration: Miller et al. in prep.), and data were required to be taken under very stable thermal conditions. It was therefore necessary to allocate thermal stabilisation periods during which the telescope kept a fixed solar attitude. Three scientific filler programmes were executed during these periods to make the best possible use of *Euclid* time. These observations resulted in three additional *Euclid* surveys, namely the Euclid Medium-Deep survey, the Independent Legacy Scientist (ILS) field, and the Euclid ecliptic survey.

The first data release (DR1) of the *Euclid* mission contains data from the following six survey components, or '*Euclid* surveys', with data acquired over three periods (PV, PDC, RSD).

- Euclid Wide Survey (RSD);
- Euclid Deep Survey (RSD, PV);
- Euclid Auxiliary fields (RSD, PV);
- Calibration fields (RSD, PV, PDC);
- PV science fields (PV);
- PDC surveys (PDC).

The contents of DR1 (Euclid Data Release 1 2026) are defined in a memo[1] approved by the Euclid Science Team (EST) and are detailed in the DR1 overview paper (Euclid Collaboration: Aussel et al. 2026b). DR1 includes all complete Level 1 (LE1) data acquired since launch until 21 May 2025. Complete LE1 data are *Euclid* raw data generated by ESA's *Euclid* Science Operations Centre (SOC) and ingested in the Data Processing System. LE1 products are fully processed into Level 2 (LE2)

[1] https://www.cosmos.esa.int/documents/10647/12245842/DR1-memo_260922.pdf/3d879dc6-d5e0-9125-54a7-f68d1b4971d8?t=1790090418174

products by the various Science Ground Segment (SGS) processing functions (PF) of the Euclid Consortium, as described in the SGS overview paper (Euclid Collaboration: Ruffenach et al. 2026) and in the PF-specific DR1 processing papers describing VIS (Euclid Collaboration: McCracken et al. 2026), NIR (Euclid Collaboration: Polenta et al. 2026), EXT (Euclid Collaboration: Corcho-Caballero et al. 2026), MER (Euclid Collaboration: Kümmel et al. 2026), SIR (Euclid Collaboration: Scodeggio et al. 2026), SPE (Euclid Collaboration: Le Brun et al. 2026) and PHZ (Euclid Collaboration: Hartley et al. 2026). We note that not all scheduled observations were successfully executed or correspond to complete LE1 data products, and not all LE1 data originated valid and complete LE2 products. There is thus a reduction in coverage from scheduled observations to LE1 data, and from LE1 to LE2 data. These differences will be mentioned throughout the paper when appropriate.

For completeness, it is relevant to mention that there is one additional component of the *Euclid* survey that is not part of DR1 or described in this paper. It is the Euclid Galactic Bulge Survey (EGBS) performed on 23 and 24 March 2025, which forms the content of the Quick Data Release 2 (Q2) and is presented in Beaulieu et al. (2026). On the other hand, the Quick Data Release 1 (Q1) data, consisting of one visit to each of the EDFs, are included in DR1, as are the data from the 17 fields observed in the PV phase for the six science programmes (Cuillandre et al. 2025) that were the subject of *Euclid* 's Early Release Observations (ERO) data release. We also note that data from Commissioning are not part of DR1 because they lack the metadata required to generate LE1 complete data products.

The RSD is computed with the dedicated `ECTile` software by the survey operations support team (SOST), a Euclid Consortium group created for the mission's operations phase that inherited the responsibilities of the ECSURV group that was active during the mission's development phase. In the development phase, prior to launch, a large number of RSDs were produced to evaluate survey scenarios and implementation strategies, against the mission requirements. During operations, the survey is re-planned a few times per year, with the computation of a new RSD. The RSDs follow a naming convention consisting of the year its first new observations are executed and an alphabetical sequence that runs through each calendar year. *Euclid*'s DR1 RSD data were acquired with observations scheduled in RSDs 2024A, 2024B, 2024C, and 2025A. Each RSD is always computed from the starting date of 14 February 2024 to the nominal end of the mission, with each version being a copy of the previous one up to a restart point; therefore RSD 2025A contains the relevant information for DR1.

The RSD is delivered to *Euclid*'s SOC that generates the operational sky survey (OSS) and the operational products required for the execution of the survey by *Euclid*'s Mission Operations Centre (MOC). In the other phases of operations, the PV phase and the PDC campaign, the scheduling was built by SOC using a different set of tools, and a manual assembly of calibration blocks.

This paper proceeds in Sect. 2 with a presentation of the process of RSD computation with the `ECTile` software, describing relevant inputs and constraints and addressing optimisation strategies and re-planning methods. The resulting DR1 RSD 2025A scheduled survey properties of the EWS, EAFs, EDFs, and calibration fields are presented in Sect. 3, where we also detail deviations of the DR1 content from the scheduled one. Section 4 describes the SOC procedures to generate an OSS from the RSD and the production of the operational products sent to *Euclid*'s MOC for the execution of the survey. The implementation of the PV phase observations and a list of the resulting PV fields is presented in Sect. 5. The PDC campaign is addressed in Sect. 6, with a description of the resulting calibration fields and of the three surveys performed during its thermal stabilisation periods. We conclude in Sect. 7 with a summary table of the DR1 *Euclid* surveys and a full-sky map showing their locations. The appendices include exposure maps of the DR1 observations of the EDFs, EAFs, main calibration fields, and PDC surveys. A list of acronyms used in the paper with a glossary of terms is also provided in the Appendix.

2. RSD computation

The RSD is built using the `ECTile` software. `ECTile` contains a set of tools developed to design, implement and analyse *Euclid* surveys. The tools relevant for the present description are three: `plan`, `wide`, and `surv`. The computation of an RSD is carried out in three stages (Euclid Collaboration: Scaramella et al. 2022). In a preparatory Stage 0, a set of input parameters is defined. After that, in Stage 1, a skeleton of the schedule of the observations of the calibration fields, EDFs, and EAFs is manually set and their exact observing dates are computed by `ECTile`. The locations of the EDFs and EAFs were carefully selected before launch Euclid Collaboration: Mellier et al. (2025). The number of visits, i.e., the number of passes over the full field, needed to reach the required depth depends on the zodiacal background at its ecliptic latitude (Euclid Collaboration: Scaramella et al. 2022). The core of the procedure is Stage 2, where the EWS is computed in a predefined tessellation.

2.1. RSD observing sequences

Each EWS, EDF, and EAF observation is made with the *Euclid* reference observing sequence (ROS), depicted in Fig. 1, and contains four dithered pointings (usually called 'dithers'). *Euclid* performs, in each dither, a VIS exposure (Euclid Collaboration: Cropper et al. 2025) in parallel with Near-Infrared Spectrometer and Photometer (NISP) spectroscopy (Euclid Collaboration: Jahnke et al. 2025) and proceeds with a sequence of observations in the three NISP photometric bands. In each dither, the spectroscopic exposure is taken with a different rotation of one of the two red grisms (RGSs), RGS000 and RGS180. The first and second dithers also include a Visible instrument (VIS) short science exposure during the NISP $Y_{\rm E}$-band observation. Prior to each NISP observation, the filter wheel (FWA) or grism wheel (GWA) assemblies are actuated and time is allocated for stabilisation at the end of the movement. In the second, third, and fourth pointings, the first activation of the wheels is done during the dither slew, allowing for a larger stabilisation time than in the first pointing. The last dither is longer, ending with a NISP dark exposure taken during the slew to the next field. The third and fourth dithers contain time allocated for VIS inline calibrations, both during NISP observations and during the final field slew. These calibrations are implemented as a fixed sequence over a 20-ROS block, consisting of alternating darks and biases (in the third dither), and alternating flats, charge injection, and vertical trap pumping (in the fourth dither). In a 20-ROS block, six are allocated for flats, six for vertical trap pumping, and eight for charge injection. Each of these calibration types then cycles over different parameter settings over a longer baseline, such that a coherent set of calibration products is generated over approximately 30 days of ROS execution. The parameter settings and the calibration types are scheduled in a way that similar cases

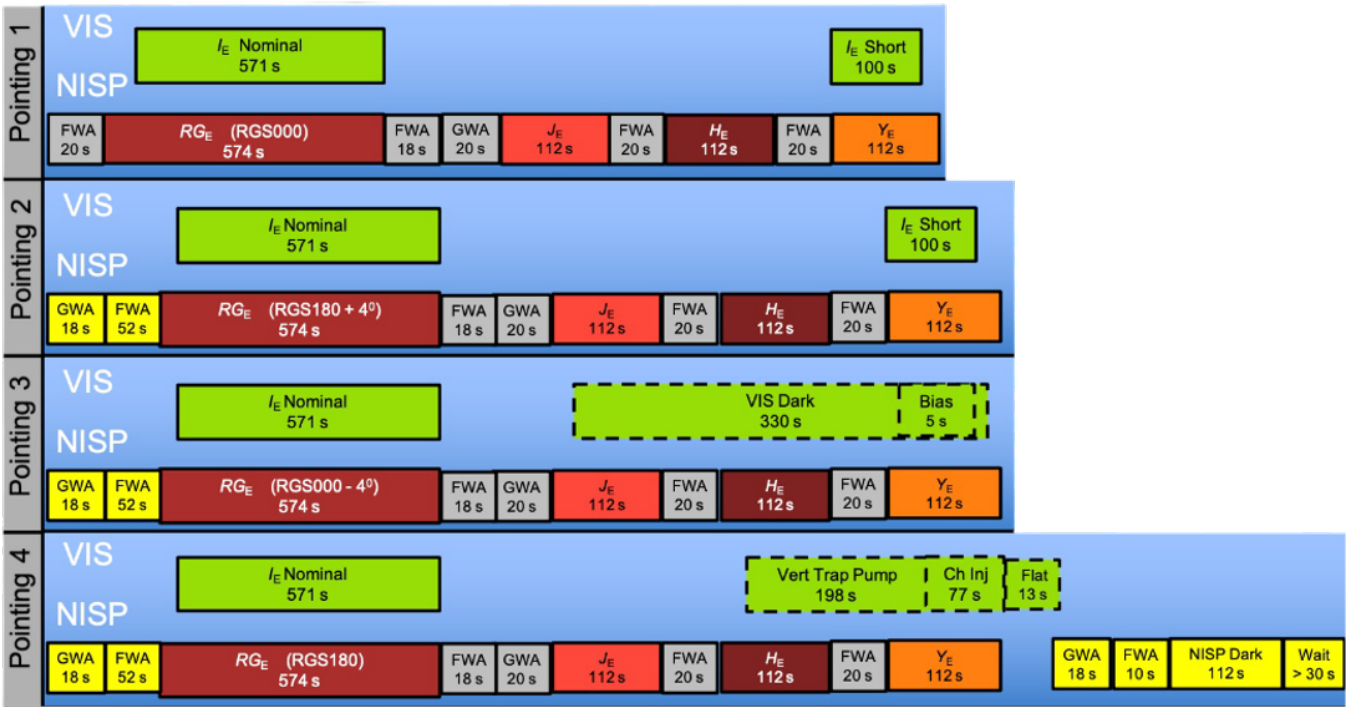


Fig. 1. ROS overview. Each of the four panels shows the timelines of the VIS and NISP activities that are carried out during one dither. VIS exposures are shown in green and NISP ones in shades of red. The times given for filter wheel (FWA) and grism wheel (GWA) include stabilisation times. The times given in VIS boxes include overheads such as shutter motion, flush, and surface inversion. Dashed boxes cycle through the various VIS inline calibrations indicated. Yellow indicate that the activities are performed during slews. The final box labelled 'Wait' has a variable time, depending on the duration of the slew to the next field. Readout, data compression and transfer activities are not included in the figure.

are spread out over the 30 days, to be resilient against the loss of consecutive observations.

The duration of the first three dithers is 996 s, excluding the 20 s lead time and the 70 s dither slews, while the fourth dither is 1006 s long. The ROS thus lasts 4204 s, excluding lead time, dither slews and the final field slew that has a minimum duration of 170 s. This implies that *Euclid* makes roughly 19 ROS observations per day.

Besides the ROS, there is also a 'ROS-blue' variant, where the blue grism (BGS), BGS000 is used in all four dithers and always in the nominal position. This variant is used in some of the visits to the EDFs and EAFs.

Calibration observations are made with special non-ROS sequences defined (see Euclid Collaboration: Schirmer et al. 2026a) in *Euclid*'s Calibration Framework (CalF). Those sequences are in general very different from the ROS, one exception being the ROS-D1 sequence that consists of the first dither of the ROS.

2.2. Stage 0: Configuration file

A long set of input parameters describing system constraints, targets properties, and survey optimisation strategy is defined in the configuration file `ectile.cfg`. The main inputs are the following.

- RSD start date and duration.
- Orbit file: *Euclid*'s orbit around L2 provided by the SOC. The orbit, i.e., the set of future positions of the *Euclid* satellite, is regularly updated as the orbit drifts and station-keeping maneuvers are performed.
- Slew thresholds and durations: there are three different types of slews (dither, field, and large) depending on the total rotation executed between two pointings. The total rotation, also known as 'eigen-slew' includes the angular distance between the pointings and the change of telescope attitude from the initial to the final position. The threshold values from dither to field slews and from field to large slews are 130.″0 and 3.°5, respectively, with the caveat that for specific calibrations field slews are allowed to be as small as 73.″0. The duration of a dither slew is 70 s, the field slews duration vary from 170 s to 283 s and the duration of a large slew varies from 5.8 minutes to around 34 minutes for eigen-slews of 180°.
- Dither pattern: the geometry of the ROS follows the shape of an 'S', with defined angular step sizes (Euclid Collaboration: Scaramella et al. 2022) and a 180° symmetry to ensure the same footprint whether an observation is made looking forward or backwards with respect to the direction of the orbital movement.
- Pointing constraints: spacecraft manoeuvrability is conditioned by two parameters, azimuth or α angle (AA) and Solar aspect angle (SAA). For a given time of observation, these two angles uniquely define the spacecraft attitude. Roughly, AA defines a rotation around the telescope boresight and SAA defines the angle between the telescope boresight and the Sun. *Euclid* is allowed to point away from the transit meridian by tilting up to 3° towards the Sun and up to 30° away from the Sun, maximising thermo-optical stability; that is, the SAA range is restricted to $[87°, 120°]$. The AA is restricted to the asymmetric range $[-2.°9, -8.°5]$, only containing negative values, which is a significant reduction of the originally intended configuration. This modification is needed to mitigate solar stray light found during commissioning; its impact on the survey is appreciable, leading to a redesign of the survey strategy, as discussed in Euclid Collaboration: Mellier et al. (2025, see also the tessellation item below).

- Region of Interest (RoI): the EWS is implemented within a region of interest (RoI), defined by the intersection of threshold lines of three sky backgrounds, namely zodiacal light, Galactic extinction, and stellar density. There are a few custom-made carvings on the thresholds to exclude the vicinity of the Galactic bulge, the Large Magellanic Cloud (LMC), the Taurus/Orion clouds, and a circle of 10° radius around the northern equatorial pole that is out of reach of the complementary ground-based telescopes. The RoI must ensure that the required average signal-to-noise ratios are achieved in all *Euclid* bands. The current *Euclid* RoI, introduced for RSD 2023A, has an area of 16 200 deg^2 distributed in four quadrants (in the shape of two large regions known as the 'mainlands' and two small regions dubbed the 'islands').
- Field of view (FoV): the geometries of the FoVs of the VIS and NISP are off-centred and do not intersect each other completely, leaving a NISP gap (Euclid Collaboration: Mellier et al. 2025). The angular extent of both FoVs and their corresponding physical dimensions in the focal plane, including the total size of their sensors (i.e, the mosaic of detectors), the size of the detectors (CCDs), and the size of the inter-detector gaps, are combined to compute a spherical rectangle observing the common FoV (rectangular area observed by both instruments). The common FoV has an area of 0.525 deg^2.
- Tessellation: the tessellation covers the RoI with tiles, small latitude-longitude rectangles, forming one compact covering per quadrant, leaving holes only in the bright stars exclusion regions. Each tile is sized to be fully observed by a FoV. For this, the tile is constructed to be larger than the common FoV, including the NISP angular gap sizes and a safety margin slightly larger than the absolute pointing error. The tile has an area of 0.551 deg^2. Due to the convergence towards the poles, the number of tiles per row decreases with latitude, and moreover they start to acquire some overlap. The natural overlap of the tessellation is around 4 %. One ROS observation of the EWS corresponds to placing the VIS and NISP FoVs on one tile of the tessellated sky and moving it along the dither S-pattern. However, the modified AA range introduced to avoid stray light forces us to observe with the telescope rotated from its natural position of AA = 0°, resulting in a FoV on the sky with a different orientation than the underlying tile. From a given observing position in the orbit, there is only a very reduced area of the sky where an AA counter-rotation can be applied within the allowed range to align the FoV with the tessellation, making it impossible to build a survey (Sect. 2.4). The solution found to solve this potential show-stopper was to accept tilted observations up to a specified threshold, as a new survey strategy. The maximum misalignment tolerated between tile and FoV position angles is a compromise between visibility and field-to-field overlap. We thus redesigned the tessellation to allow for a maximum FoV-tile misalignment of 3.°5. The main impact in the tessellation is that the tiles need to be placed closer together to avoid gaps due to the tilt. Through an analysis of the number of counts at pixel level, we determined the optimal distance between the centres of the tessellation tiles. The resulting tessellation has a mean tile overlap of 14 %, a significant increase from the original 4 %, which causes a significant decrease in surveying efficiency and therefore in the total area at the nominal end of the mission (although it also means that the data are generally a little deeper than planned). This tessellation was first used in RSD 2024A.
- Polar caps: due to the tessellation convergence at the ecliptic poles, high-latitude tiles cannot be observed in a way that is compliant with the pointing constraints. Local tessellations are thus introduced in the polar caps, defined by the two thresholding ecliptic latitudes of ±77.°8. The two polar caps are covered with 22 sectors, each with its own local tessellation.
- Bright stars avoidance: a catalogue of stars brighter than 4 AB magnitudes in any of the *Euclid* photometric bands, together with exclusion radii to be applied to avoid harming the detectors, and information on proper motions.
- Planet avoidance: observations must avoid pointing too close to the outer planets. Angular avoidance radii are specified in the mission requirements.
- Observing timings: defined for all elements of each observing sequence, including the ROS and special sequences for calibration fields.
- Targets table: including, for each field, the location, position angle, pattern geometry, number of visits, type of pointing smearing applied between visits, ratio of blue/red grism visits and observing sequence.
- Scheduling optimisation: several parameters controlling various aspects of the scheduling, such as patch margins, RoI clipping, quadrant corners, or patch selector, can be defined (these parameters will be described in Sect. 2.4).
- Ground-based surveys: the footprints of the surveys providing Euclid DR1 complementary data, which are the Dark Energy Survey (DES) in the southern sky (Abbott et al. 2021) and the Ultraviolet Near-Infrared Optical Northern Survey (UNIONS) in the north (Gwyn et al. 2025).
- Special operations (SOPS): periodic interruptions of the survey observations are scheduled to enable non-survey operational activities, such as orbit adjustment, reaction-wheel momentum offloading, or instrument maintenance. SOPS used to require 12 hours, but in RSD 2025A, applicable to DR1, the duration was reduced to a 6 hour time-slot for SOPS every 4 weeks on Mondays at 12:00 UTC (within a margin of 2 h). More recently, the cadence decreased and RSD 2026A schedules the SOPS 6 hour interruptions only every 8 weeks on Wednesdays at 15 h UTC (with a −2 h, +11 h margin).

2.3. Stage 1: Scheduling targets

The next step in computing a reference survey is to design a schedule for all observations that are not part of the regular EWS. These include all the EDF and EAF observations, all of the calibrations with the exception of the PSF block defined below, and all the polar cap sectors. The detailed description of the process given in Euclid Collaboration: Scaramella et al. (2022) is still valid, with the caveat that there have been a few modifications in calibration specifications and the introduction of new calibrations.

The complete overview of the DR1 calibrations is given in Euclid Collaboration: Schirmer et al. (2026a). It contains 13 calibration observation blocks, labelled CALBLOCK-F-001 and 007 through 018. Each calibration block fulfills various calibration products for one or both instruments. F-001 (self-calibration) is observed with a single-dither ROS (ROS-D1), while the others are observed with special sequences. Observations with similar cadence requirements are scheduled together, forming monthly blocks (F-001, F-018, F-007), biannual blocks (F-009, F-016, F-011), and PSF blocks (F-012, F-015, F-013, F-008). CALBLOCK-F-002 through F-006 are reserved for ROS

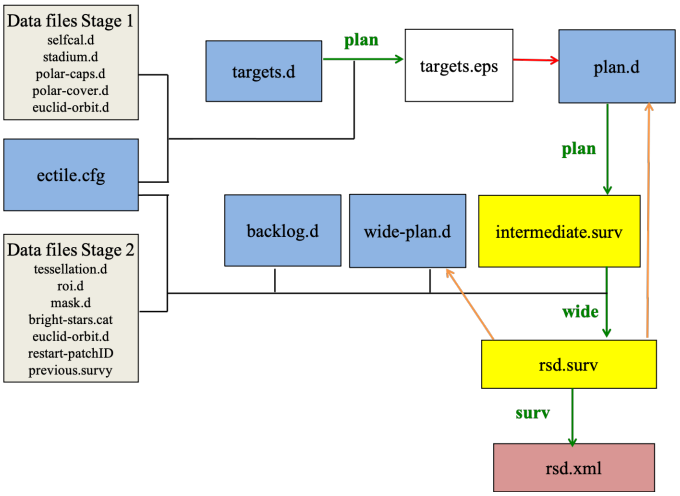


Fig. 2. Schematic representation of the `ECTile` pipeline for computing an RSD, showing the main tools and files. The configuration file and input data needed in Stage 1 and Stage 2 are shown in the left. The procedure flows with the green arrows. An `ECTile` tool named in green next to an arrow is applied to an input file, and uses information from the configuration and data files connected with black lines to produce an output. Output binary files are shown in yellow and output plots in white. A red arrow indicates that the output is manually constructed using information of the previous file and not automatically computed by an `ECTile` tool. Blue boxes are the five core input files that are manually modified by the mission planner and are the stepping stones of the RSD computation. The orange arrows indicate the optimisation loop: the monitoring on-screen of the step by step computation of the RSD guides the mission planner in the manual modification of the files `plan.d` and `wide-plan.d`. At the end of the process, the final RSD file is generated in Extensible Markup Language (XML) format (brown box). See text for a description.

observations: F-002 for EDFs, F-003 for the completeness and purity calibrations (CPCs) are made with observations in the EDF-N and EDF-S at fixed cadences to obtain a range of observing directions for the spectroscopic data; F-004 and 005 for observations of the EAFs used, respectively, for colour gradient and photometric redshift calibrations; and F-006 for the EWS.

Stage 1 is a process that is mostly manual and is done in two steps. Summarising the description of Euclid Collaboration: Scaramella et al. (2022) and referring also to Fig. 2, in the first step composite targets are assembled by combining one or more targets. The list of composite targets is stored in the file `targets.d`. The composite targets defined in this file form the set of all possibilities that will be available for scheduling and their definition is an optimisation choice. The `ECTile` tool `plan` computes a visual chart (`targets.eps`) of the visibility window of each composite target given as an interval of the Sun's ecliptic longitude, showing also the duration of each observation within the interval. From this information the mission planner moves to the second step, manually constructing an observing plan (`plan.d`), known as the calibration plan, by placing each composite target in six ordered sequences (one per year) according to the Sun's longitude of their visibility windows. As an optimisation strategy, various composite targets are grouped together in a block to be observed back to back. In this case, one of the targets is assigned the role of anchor and the observing longitudes of the neighbouring targets are shifted (within their visibility windows) to ensure no time gaps exist between the targets of a block. The placement of the composite targets is a core aspect of strategic planning of an RSD. It is made with two goals in mind: (i) respecting requirements on cadences and priorities; and (ii) building a plan that enables an optimal implementation of the EWS in the next stage, avoiding leaving survey windows that are too small and ensuring that the EWS coverage in the first year (where many calibrations need to be scheduled) is capable of reaching the expected area for DR1. The calibration plan is best populated iteratively, adding the highest priority first and then adding the rest in decreasing order of difficulty, clustering them whenever possible. Here, 'difficulty' refers to the width and availability of the visibility windows. The most difficult targets have a single possible visibility window. Most targets have two visibility windows but, in some cases, these can be very short, hindering their clustering. The plan is then executed by the `ECTile` tool plan that generates the intermediate survey file (`intermediate.surv`), where the longitudes are converted to time assuming the given starting date. The result does not follow `plan.d` strictly but performs optimisation steps by automatically making small shifts in time and merging neighbouring blocks of targets according to optimisation parameters defined in `ectile.cfg`.

2.4. Stage 2: Computing the EWS

The survey windows available to schedule the observations of the EWS correspond to the time intervals left unscheduled in Stage 1 between two consecutive target observations. The process of constructing the EWS schedule is described in detail in Euclid Collaboration: Scaramella et al. (2022). In the following, we provide an overview of the process, also referring to Fig. 2.

The method proceeds by gradually scheduling each survey window in chronological order. The `ECTile` tool `wide` takes the `intermediate.surv` file as input and computes the visibility windows for all orbital positions of the spacecraft during the dates of the first survey window. The set of visibility windows shows the tiles that are within reach in a given survey window. The limitations on the range of the two solar angles, SAA and AA, together with the need to keep the fields aligned with the tessellation (within the tilting margin, cf. Sect. 2.2) determine the shape of the visibility window.

Figure 3 shows the visibility window, represented as the reach in ecliptic longitude around the transit ecliptic meridian as a function of ecliptic latitude. It is valid for any point in the orbit, with the caveat that the transit meridians vary with orbital movement. We note that since the AA range no longer includes zero, the transit meridian is barely within reach and observations with SAA = 90° are no longer the norm as they were in the original pre-launch designed survey strategy. From any point in the orbit, there are more precisely two visibility windows in the sky:

- leading, when observing in the leading direction, i.e., when looking forward in the direction of the orbital movement;
- trailing, when looking in the trailing direction, i.e., looking back with respect to the orbital movement to the antipodal side of the sky and with the telescope flipped around its axis.

Given the asymmetries of the SAA and AA allowed ranges, each of the two visibility windows has two distinct sections, one in the northern and the other in the southern hemisphere. The broader section, indicating longer visibility, is in the north when looking in the trailing direction and in the south if looking in the leading direction. Given the shape of the RoI, only one of the two sections of each visibility window lies on a mainland. From these considerations it follows that if at a period of time the broad section of the leading window lies in a mainland, the broad section

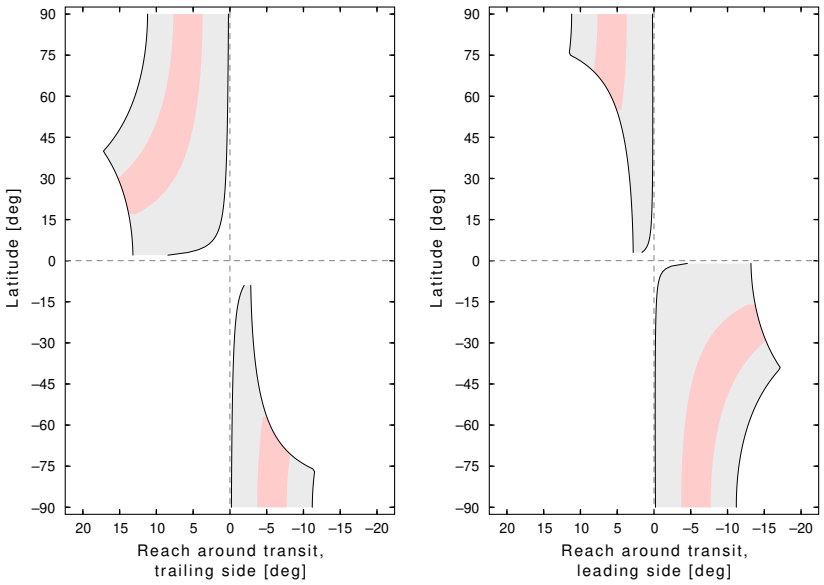


Fig. 3. Visibility windows for trailing (*left panel*) and leading (*right panel*) observations from any point of the orbit, computed for the SAA and AA allowed ranges and a maximum misalignment of 3°.5 between the observed fields and the tessellation. The leading and trailing transit meridians are separated by 180°. The inner pink bands show the visibility windows computed for the same SAA and AA ranges but with no tilt allowed, illustrating the unfeasibility of computing a wide survey in those conditions.

of the trailing window necessarily lies in the other mainland. This defines a so-called summer season where the visibility is longer and it is easier to schedule EWS observations. In contrast, there is another period of the year in which the two narrow sections of both visibility windows lie on the mainlands. This epoch is dubbed the winter season, where visibility is simultaneously short on both mainlands and the progress of the EWS is therefore difficult.

Figure 3 also shows the visibility windows in the case where misalignemnts between FoVs and tiles are not allowed. In this case, the only regions reachable are the ones where it is possible to use the allowed range of AA to counter-rotate a misaligned FoV, such as to align it with the tessellation. As shown in the figure, those regions are extremely narrow. Conversely, allowing for larger misalignements between the observed fields and the tessellation would result in larger visibilities. In the extreme case of having no tessellation, i.e., observing with unconstrained position angles, as is the case of most stage 1 observations, visibility is solely determined by the SAA range, broadening towards the poles where visibility is perennial. The drawback of such approach would be to create gaps between observed fields, which would require a procedure to be filled in, either with additional observations or by placing the centres of the tiles closer to each other, in any case leading to a decrease in survey efficiency. The optimal value of maximum misalignment is the one that, even though introducing a highly constrained visibility, it still allows us to observe fields all year round and throughout the RoI, with minimal field overlap such as to keep the survey efficiency large enough to enable the EWS to reach an area close to the requirement in the nominal mission duration.

Proceeding now with the description of the scheduling process, for the first survey window, and as a function of its duration, `ECTile` generates a set of patches that are possible to observe within the available time, a patch being a connected set of tiles of the tessellation. Usually, it generates at least one patch from each mainland and sometimes also from the islands. One of the patches is subsequently selected, and the others are discarded. The generation and selection of patches are done automatically according to a hard-coded heuristic.

- Priority to higher latitudes: promoting a contiguous build-up of the EWS layer by layer from the ecliptic poles (where the sky quality is higher) towards the equator, trying to complete two layers (one per hemisphere) longitudinally in roughly 1 year before moving to the next one.
- Minimising solar angle variations: this conditions the height of a patch, which depends on the speed of the orbit and duration of the ROS.
- Priority to the mainlands over the islands: promoting larger contiguous coverage.
- Preference for areas covered by DES and UNIONS footprints: DR1 RSDs prioritise southern versus northern hemisphere due to earlier availability of DES data.

Once the patches are selected for a survey window, a search is made to find PSF calibration fields within reach from those patches. If the search is successful, an observation of a PSF field (plus the other calibrations associated in the PSF block) is scheduled within the survey window, with SAA and AA values matching the ones of the contemporary EWS patch. The purpose of scheduling the PSF fields in stage 2 and not in stage 1 together with the other calibrations is to ensure matching solar angles, since the PSF varies with the thermal conditions. SOPS interruptions are also scheduled at this stage. These various placements use some of the time of the survey window, hence leaving less time for the scheduling of the patch and, thus, the patch originally selected is reduced by a few tiles. The final list of tiles within the patch are geometrically connected by the scheduling algorithm, known as the diffusion algorithm (Euclid Collaboration: Scaramella et al. 2022), and time stamps are assigned to each tile taking into account the starting time and the slew time. The tiles are observed in a sequence that minimises solar angle variations. The process continues to the next survey window; a RSD contains around 100 survey windows. Given that *Euclid* observes roughly 19 ROS tiles per day, a single patch in a typical survey window of 10 days contains up to around 200 tiles.

In addition to the patch generation and selection heuristics, there are other parameters, with default values set in `ectile.cfg`, that control the many aspects of scheduling, with the goal of minimising the risk of the diffusion algorithm to fail. These parameters control the following four mechanisms.

- RoI clipping: at the start of the process some areas of the RoI are masked with rectangles, effectively reducing its footprint,

to help the diffusion algorithm with a smoother input geometry. As the EWS builds, it is sometimes useful to mask out additional areas to steer the patch placement towards certain areas.
- Quadrant corners: the diffusion algorithm fails if the shapes of the patches are not approximately rectangles. To enforce this shape, patches near the corners of the RoI quadrants are partitioned into segments. The coordinates of the relevant points, both at the bottom and at the sides of the RoI quadrants, are stored for this purpose. As the EWS builds up and more patches are placed, new sharp corners may appear in the evolving top layer of the footprint. If they are found to cause a scheduling failure, their coordinates can be added to the list of quadrant corners to enforce patch partitioning at the new critical points.
- Patch selection: in the first survey windows, there is no valid reason to choose one patch over the other. However, later on, the heuristics for choosing the best patch are not so effective, and it is useful to have a mechanism to override the default selection.
- Shrinking margins: to embed some scheduling margin into a generated patch, its allocated time is decreased by some margin. Default margins are applied to the individual partitions of a patch and also to the total time extent of the patch.

At each iteration, the evolving survey map is updated on-screen, adding the resulting scheduled patches of the current iteration. Often, patches show imperfections. Common types of failures are the generation of patches that do not use the full time available in the survey window, creation of patches with irregular shapes that will be difficult to fit with the geometry of neighbouring patches, or the existence of a small set of tiles left unscheduled between two patches. The mission planner can try to fix the issues by changing the default values of the scheduling parameters for the problematic iterations. The general strategy is to make a full run of the process over the whole survey windows, analyse it to identify iterations where the default choices were not the best, and act at two levels.

- Customised patch selection. The patch selection of a given survey window can be overridden by selecting a patch from a different quadrant. The new selection is defined in the file `wide-plan.d`.
- Customised shrinking margins. It is possible to define alternate specific shrinking margins for selected iterations in `wide-plan.d`. Shrinking margins are specified as a duration, later converted to units of longitude and lead to a modification in the patch width and height, or in a longitudinal shift of its location.

Sometimes, these mechanisms are not capable of fixing the issues. In those cases, an alternative is to change the size of a problematic survey window. For this, the mission planner goes back to `plan.d` and shifts a target, either by slightly delaying a calibration block or by a major edit of the calibration plan. This proves to be an effective way to avoid the presence of vertical and narrow gaps of unobserved tiles. Another useful approach is to use the fact that EDF-N has perennial visibility, to place its visits in the observing plan where they conflict the least with the EWS survey windows. This strategy was applied in the DR1 RSDs, but it will not be available in future RSDs since the EDF-N visits are required to be finished by DR2. We note that a modification in `plan.d` implies restarting the process from scratch.

In summary, the computation of the EWS is a laborious and time consuming procedure. A single run of the `wide` tool is relatively fast and fully automated. However, a single run is not enough. Most often, the result contains many shortcomings or low performance. The survey windows can then be optimised using the various mechanisms described above. The optimisation must be done in chronological order, since a change in one iteration may potentially change any of the subsequent windows. A new run must hence be made after each modification, until the final survey window is optimised. At that point the RSD survey is complete in the form of a binary file (`survey.sur`) and the `surv` tool is applied to it to generate the RSD in the official format (`rsd.xml`).

2.5. Survey replanning

A new RSD is computed regularly. There are various reasons for survey replanning, including:

- to reschedule skipped observations that have been dislodged by other activities (such as ice decontamination campaigns);
- to reschedule skipped observations not executed due to instrument outages;
- to reschedule lost observations with low quality flags (such as observations affected by solar activity or ice contamination);
- to implement updated calibration specifications;
- to implement updated system requirements;
- to include additional observations (such as implementation of the Quick Data Releases programmes);
- to implement science optimisation strategies;
- to implement recommendations from mission reviews.

During the replanning cycle, SOST tracks various sources of survey-monitoring information, including the SOC's table of events, and feedback from various interfaces, such as the SGS processing, the science coordination group, the CalF, the Mission Manager, and the EST, and compiles a list of replanning items.

Survey replanning is the process of computing a new RSD from a previous one, by retaining all the observations up to a restart date, also called the break point, and computing an observation schedule for the remaining nominal survey time. Given the incremental nature of the survey computation, where a plan is computed by iteratively appending observations, a change in one target observation or in a survey window invalidates all the rest of the survey, implying a computation of the full survey after the specified breakpoint. Note also that not all aspects of a survey can be subject to replanning. Some parameters were set when building the first operational survey and must not be changed throughout the mission. These are:

- the RoI, since a modification would imply a new tessellation, invalidating the tiling associated with previous observations;
- the tessellation;
- the definition of the polar patches, since changing this would impact the shape of all other polar patches, invalidating the already acquired polar patches;
- the EDF-S shape.

In replanning, the restart date is specified by the index of the first patch of the previous survey to be changed. Everything up to that point is copied from the previous survey, while everything from that point onwards is up for replanning. The restart patch may be an EWS patch or any patch from the calibration plan. The replanning process starts with the computation of a new calibration plan, editing the `plan.d` file after the break point to implement the required changes. All the three files `ectile.cfg`,

`targets.d`, and `plan.d` may be edited for the purpose of replanning. This means that the Stage 1 replanning may include new targets, rescheduling of fully or partially lost targets, and new timings and cadences in the calibration plan. Then, the plan is converted to a schedule as usual, with the `plan` tool, generating the intermediate survey.

The computation of a replanned EWS requires the definition of new patches, named 'infills', which will cover the lost and skipped fields of the previous survey, i.e., the gaps. An infill patch is a sequence of observations (one or more consecutive obsIDs) that has been previously scheduled. The infill patches are treated as new targets. They are registered in a new input file, `backlog.d` (cf. Fig. 2), with each infill patch being defined as a specified sequence of obsIDs of the previous survey. An infill patch will behave like any other target and its visibility can be determined with the usual `ECTile` tools. In some cases, infill patches are inserted in the calibration plan, in their corresponding visibility locations. This capability is best suited for small infills and is particularly useful in those cases where the visibility of an infill falls in the middle of a calibration block (and not inside a survey window). However, in most cases, it is more convenient to insert them into a survey window during the Stage 2 procedure. For this, each infill is registered in `wide-plan.d` as part of a survey window, and is declared as being large or small. In the presence of infills, the processing of a survey window is modified from the standard procedure described in Sect. 2.4. The first operation is now to place the large infill as a new patch, either at its natural placement or shifted according to the margin parameters.

This placement splits the survey window into two subwindows. Only after that are the EWS patches generated and selected in the usual way. Then, small infills, if any, are placed by carving time in the survey window, just like the PSF and SOPS are inserted at the end of the iteration step. Finally, we note that gap-recovery should be handled as early as possible in the schedule to reduce the chance of gaps piling up and to keep the re-observation dates as close as possible to their original observations. We also stress that when computing the survey statistics, the pre- and post- breakpoint RSD information is merged, avoiding multiple counts of the corresponding observations.

Survey replanning was first used in the computation of RSD 2024C from RSD 2024B, although no re-observation of EWS patches was made at the time, i.e., RSD 2024C did not schedule any infills. The re-observations were only introduced in the calibration plan. Later on, the computation of RSD 2025A from RSD 2024C was the first time that replanning was made with EWS gap recovery. The first modified RSD, RSD 2024B, was computed in a different way and is a repairing of the original RSD 2024A rather than a fully replanned survey.

The repairing process computes a new survey from a previous one from a breakpoint onwards, by applying just a small set of changes to calibrations. The calibrations are scheduled in the same order as in the previous survey, but implemented with the updated parameters. The allowed modifications are minor changes of on-target timings, causing a calibration to last slightly more or slightly less than previously scheduled. Other changes are also possible, such as the number of pointings of a calibration, the pattern covering a calibration field, or the grism cycling of certain calibrations. The EWS sequence of observations is left intact, but each tile is observed at a slightly different time, due to the drift in the survey window timings. The EWS patches are regenerated with updated orientation and solar angles. Given the very limited visibility of the EWS tiles, the repairing procedure is successful only if the drift is kept to a minimum, with a total cumulated drift over the full survey of a few hours at most. PSF calibrations and SOPS are recomputed from scratch and repairing is done one iteration at a time, in chronological order.

3. RSD DR1 components

3.1. RSD DR1 definition

The first operational RSD, RSD 2024A, started to be executed on February 14 2024. At that time, thin layers of water ice were already forming on optical surfaces due to outgassing, causing a reduction in transmission (Euclid Collaboration: Schirmer et al. 2023). Selective heating was applied to folding mirror FoM3 and to mirror M3, followed by recalibration activities. This decontamination campaign lasted 9 days, from 12 to 21 March 2024. All observations previously scheduled for this period were calibrations and were not required to be rescheduled. In a first moment, the decontamination restored the transmission to immediate post-launch levels. However, after an initial improvement, VIS data started to quickly degrade and on 6 June 2024, a second selective heating of folding mirror FoM3 was performed (Euclid Collaboration: Schirmer et al. 2026b). The second decontamination campaign was carried out during 5.5 days ending on 12 June 2024, and this time the scheduled polar cap north-cap-06 and 8 EWS tiles were skipped and were rescheduled in a new RSD, although not in time for DR1. No other decontamination campaign has been required so far. VIS data observed between the two decontamination campaigns, from 23 March to 7 June 2024 were declared invalid. This period, which became known as the 'ice age', was rescheduled in RSD 2025A for re-observations executed with the ROS, although NISP observations had not been declared invalid. In total, the DR1 RSD revisions consist of the following replanned RSDs:

- RSD 2024B (operating from 15 July 2024), repairing of RSD 2024A, with no rescheduled observations;
- RSD 2024C (operating from 16 November 2024), replanning of RSD 2024B, rescheduling EDF-N (one visit), CPC-N (one visit), and polar-cap (one patch);
- RSD 2025A, replanning of RSD 2024C (operating from 28 February 2025), rescheduling EDF-N (three visits), CPC-N (four visits), polar cap (three patches), EAFs (one visit to COSMOS), and infills (12 patches, totalling 1119 tiles mostly from the ice age).

DR1 includes the various types of observation scheduled in RSD 2025A and executed in the 462.8 days that occurred between 14 February 2024 and 21 May 2025. Four of those days were reserved for SOPS and 1.2 days were allocated to the EGBS, presented in Beaulieu et al. (2026), whose data were released in Q2. In the remaining 457.6 days, the RSD scheduled visits to EWS tiles, EDFs, EAFs, and calibration fields. The DR1 schedule is depicted in the timeline shown in Fig. 4, where each observation type is represented by a unique colour.

Not all RSD 2025A observations executed up to 21 May 2025 are part of DR1, because some are not complete or were declared invalid. There are five reasons why some observations are excluded from DR1. These are the following.

- Ice age: all observations from the ice age period are declared invalid.
- Ground-based data: EWS observations without external ground-based data are considered incomplete, since ground-based data are necessary to retrieve photometric redshifts within requirements for the weak lensing probe. In the southern sky, DES (Abbott et al. 2021) is currently used until

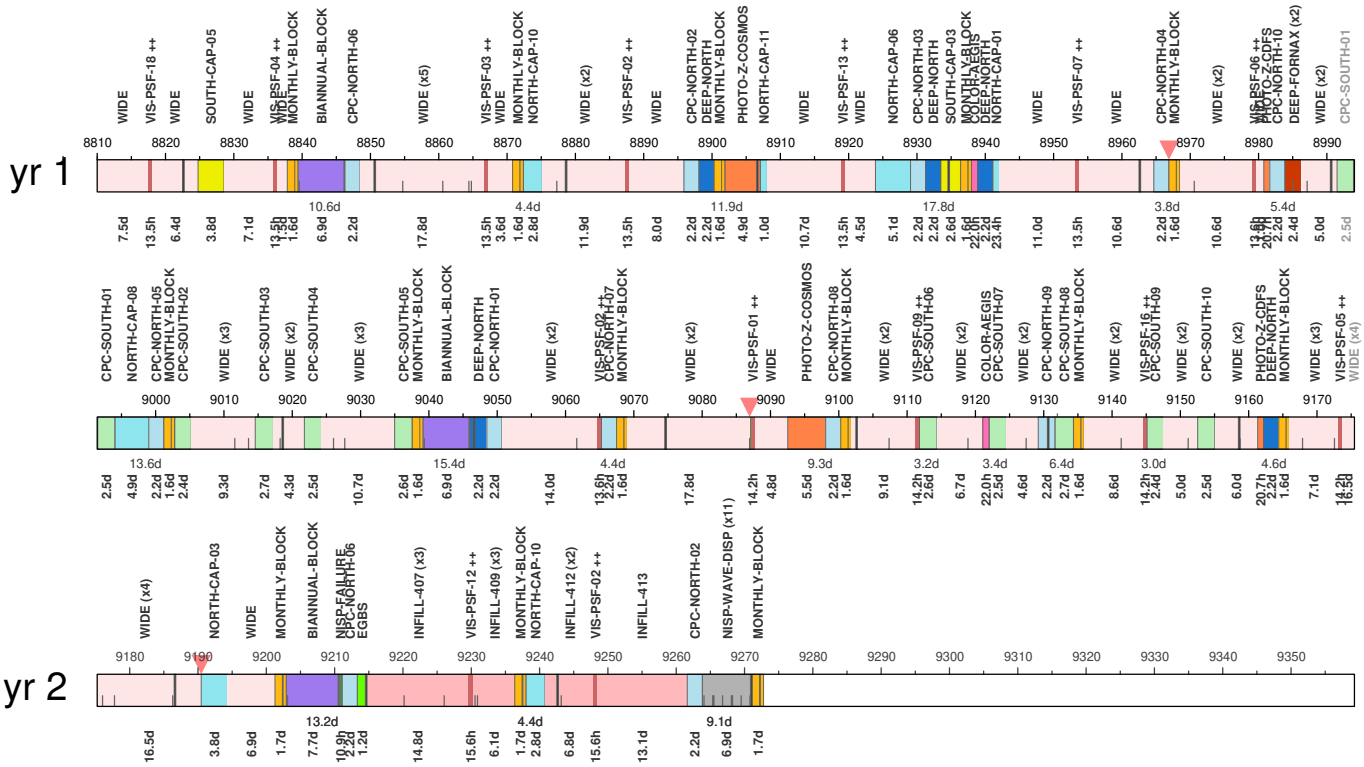


Fig. 4. DR1 RSD schedule timeline, from 14 February 2024 to 21 May 2025. Each EDF, EAF, and calibration block observation is shown as a box of a unique colour, labelled by the name and duration of the observation. Vertical black lines are the SOP time slots. The running time scale above the boxes is the MJD2000 date. The pink boxes are the survey windows where EWS observations are scheduled, the ones in a darker shade labelled 'infill' are re-observations of previous ice-age EWS observations. Colour bars under the EDF and EAF boxes indicate when red or blue grisms are used. Orange triangles mark the starting point of a new RSD (RSD 2024A, RSD 2024B, RSD 2024C and RSD 2025A), and the blue triangles mark the equinoxes, which is relevant information for scheduling.

deeper data from the Vera C. Rubin Observatory Legacy Survey of Space and Time (LSST; Ivezić et al. 2019) become available. In the northern sky, the coverage is provided by UNIONS (Gwyn et al. 2025), including a UNIONS extension, except for the most southern part, which is expected to be covered by Rubin's LSST. These observations will become complete once the ground-based observations will be available.

- Instrument outage: observations lacking data from one of the instruments are considered incomplete. There were some instances of the instruments being turned off preemptively, to avoid any instrument damage.
- Non-executed observations: there are cases of scheduled observations that were not executed, e.g., due to on-board tests or to give room for decontamination activities.
- RA = 0 h: observations whose pointings cover the RA = 0 h line cannot yet be processed by the SGS and are temporarily considered invalid. This issue is fixed in the DR2 pipeline.

During the observing period of 457.6 days, 46.8 days are spent slewing either between dithers or from field to field. In this period, the RSD contains a total of 11 697 observations. All observations comply with the solar angle restrictions, with AA kept in the range −8.°28 to −3.°06 and SAA in the range 87.°16 to 113.°0. The map of (elevation, AA) values for each RSD pointing is shown in Fig. 5, where elevation is defined as 90° − SAA. Most of the EWS pointings are close to zero elevation, indicating that they are observed near transit. This is a feature of the first year of the survey; in later years a longer reach in longitude will have to be applied to cover gaps in the sky that were left unobserved in the first orbits. The full allowed range of SAA is only used for CPC-S observations. These are EDF-S observations made with a required cadence, and they often need to be observed far from transit to comply with the cadence. Each visit to the EDF/CPC field is made by keeping their tiles aligned and applying an AA rotation to compensate for a varying SAA, which leads to a strong correlation between the two angles.

3.2. The Euclid Wide Survey

The RSD 2025A EWS contains 5384 ROS observations, corresponding to 21 536 pointings. We note that *Euclid* observations are identified by a unique number: the 'obsID', with each ROS observation being assigned a single obsID for the four dithers. The area of the EWS footprint is 2639.1 deg^2. This area already excludes gaps left around bright stars that amount to 60.5 deg^2. A significant fraction of this area is not processed by the SGS and is excluded from DR1 for the reasons listed above. The breakdown of the excluded observations is as follows.

- Ice age: during the ice age, a total of 1166 EWS obsIDs were executed on the *Euclid* tiles, consisting of 1092 tiles from the tessellation and 74 from polar patches. All were declared invalid and their observations were rescheduled. 838 of these tiles were reobserved in RSD 2025A and their data are part of DR1. Therefore, only the remaining 328 obsIDs, reobserved at a later time, contribute to a decrease in the EWS released area of 147.4 deg^2, of which 9.7 deg^2 is in a polar patch.
- Ground-based data: in the southern hemisphere, when following the strategy of observing in latitude layers from the

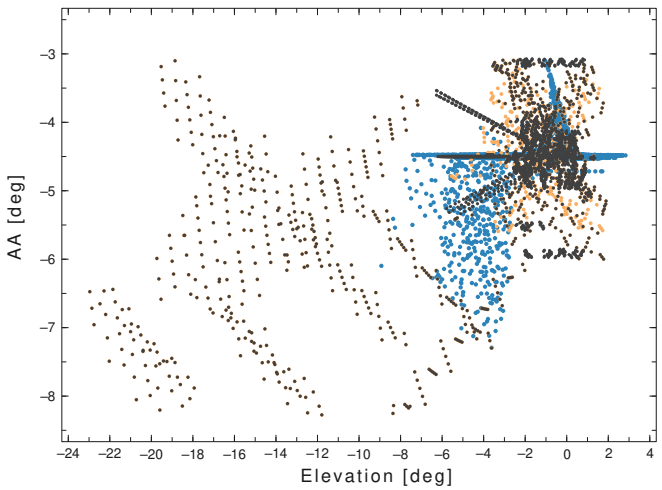


Fig. 5. Solar angles map of the DR1 RSD pointings. The SAA value is represented by the Elevation, which is defined as 90−SAA. Each point represents an observation: EWS (orange); EDS and EAF (blue); CPC (brown); and calibrations (black).

ecliptic poles to the equator, the telescope passes areas of the RoI that are not covered by DES. Some of these areas were nevertheless observed to avoid creating large holes in the contiguous coverage early in the mission. These data need to be excluded from DR1 while waiting for LSST data. The excluded areas due to non-existing ground-based data amount to 302.3 deg^2 in 633 tiles.

- Instrument outage: there were five instances of instrument outages, leading to incomplete data. Recovery from an instrument outage requires manual intervention and is only possible once every 24 hours, during the daily telecommunication period. This affected 53 EWS tiles, corresponding to 25.4 deg^2 of excluded area.
- Non-executed observations: during this period, a total of 124 EWS scheduled obsIDs were not executed due to various reasons, including a delay in the start of the survey that prevented the execution of obsIDs 1 to 6, on-board testing that replaced ObsIDs 7192 and 7193, and, most importantly, the second decontamination campaign that postponed the observation of the large polar-north-06 patch. The corresponding excluded area is 56.5 deg^2.
- RA = 0 h: there are 39 tiles that cross the meridian and are excluded from DR1. 22 of them are already excluded for having no ground-based coverage and therefore the additional excluded area is only 8.2 deg^2.

Given these considerations, the resulting DR1 EWS area totals 2099.3 deg^2, unevenly distributed in the two ecliptic hemispheres:

- Northern mainland: 560.7 deg^2,
- Southern mainland: 1538.6 deg^2,

which represents a decrease of 539.8 deg^2 with respect to the RSD EWS scheduled area. The EWS area validated for Level 2 data by the relevant SGS Organisation Units (OUs) is further reduced, with Euclid Collaboration: Aussel et al. (2026b) quoting a EWS DR1 SGS-validated area of 1900 deg^2. Part of the additional area reduction is due to radiation impact related to solar activity. There are, in particular, 94 EWS obsIDs with the four dithered frames impacted that are already scheduled for re-observation at a later time. The set of identified obsIDs is 8–14, 2757–2774, 3802–3812, 4861–4875, 5644–5660, 6580–6586, 7040–7052, and 7074–7079. They contribute to a decrease in the effective useful EWS area of 44.5 deg^2.

Figure 6 shows the EWS DR1 footprint, including the DR1 valid and complete area, and also shows the various types of excluded regions. The non-EWS components of the DR1 RSD, i.e., the EDF, EAF and calibration fields observed in DR1 (see Sect. 3.3), are also shown. We note that the remaining fields observed in DR1 corresponding to the non-RSD components of the *Euclid* surveys described in Sects. 5 and 6 are included in the full DR1 *Euclid* surveys map shown in Sect. 7.

3.3. The Euclid RSD targets

The remaining 6313 observations correspond to the EDFs, EAFs, and calibration fields mentioned in Sect. 2.3, here grouped under the title 'RSD targets'. EDF and EAF observations are made with the ROS, with one observation (with 4 dithers) corresponding to one obsID. Calibration fields are observed with non-ROS special observing sequences consisting on many pointings (typically much more than 4), but that are assigned a single obsID for the full sequence (with a few exceptions). For calibration observations, the quoted number of observations corresponds to individual pointings, therefore, unlike for the ROS observations reported in Sect. 3.2, the number of corresponding obsIDs is much lower than the quoted 6313 observations.

Table 1 summarises the EDFs and EAFs observed for DR1, showing the coordinates of their centres, areas, and number of visits. Since each visit is made from a different position in the orbit, each visit has a different position angle on the sky. This implies that the overlap is maximum at the centre of the field, decreasing towards the edge, and thus the area with at least one visit is much larger than the central 'design' area, which is the one that will reach the full depth at the end of the mission. The difference between the 1-pass and the full-depth areas is smaller in the case of EDF-F, due to its lower ecliptic latitude, and therefore shorter visibility, which strongly constrains the range of allowed observation positions in the orbit. We note that one visit represents one pass over the full field, thus containing a large number of obsIDs, depending on the size of the field. The total number of planned visits is also given, providing an indication of the current progress towards full depth. The total number of visits to reach full depth is a function of ecliptic latitude, to compensate for the higher sky background at lower latitudes. We also note that during one of the EDF-N visits included in DR1 (patchID 44), there was a VIS instrument outage and half of the VIS data from that visit was lost. There were a few other visits lost (incidentally always in EDF-N), but those were fully discarded.

The EDS is executed on the three EDFs, and corresponds to 1271 obsIDs. The EDFs are observed either with the standard ROS that uses the RGS grisms or with the ROS-Blue variant, where all the four dithered frames acquire the spectroscopic data in the same direction using the BGS grism. The number of visits in Table 1 discriminates between 'red' (denoted R) and 'blue' (denoted B) visits. The goal at the end of the mission is to achieve a 5:3 blue-to-red ratio. The ratio at DR1 is very far from the goal, with a significantly large number of red visits. This is due to the need of performing the first ten EDF-N visits, as well as the first ten EDF-S visits, with the RGS in order to obtain as soon as possible a CPC sample compatible with the EWS observing mode.

Additional data on the EDF-N and EDF-S fields were taken in the PV phase and are also included in DR1 (see Sect. 5.2). We

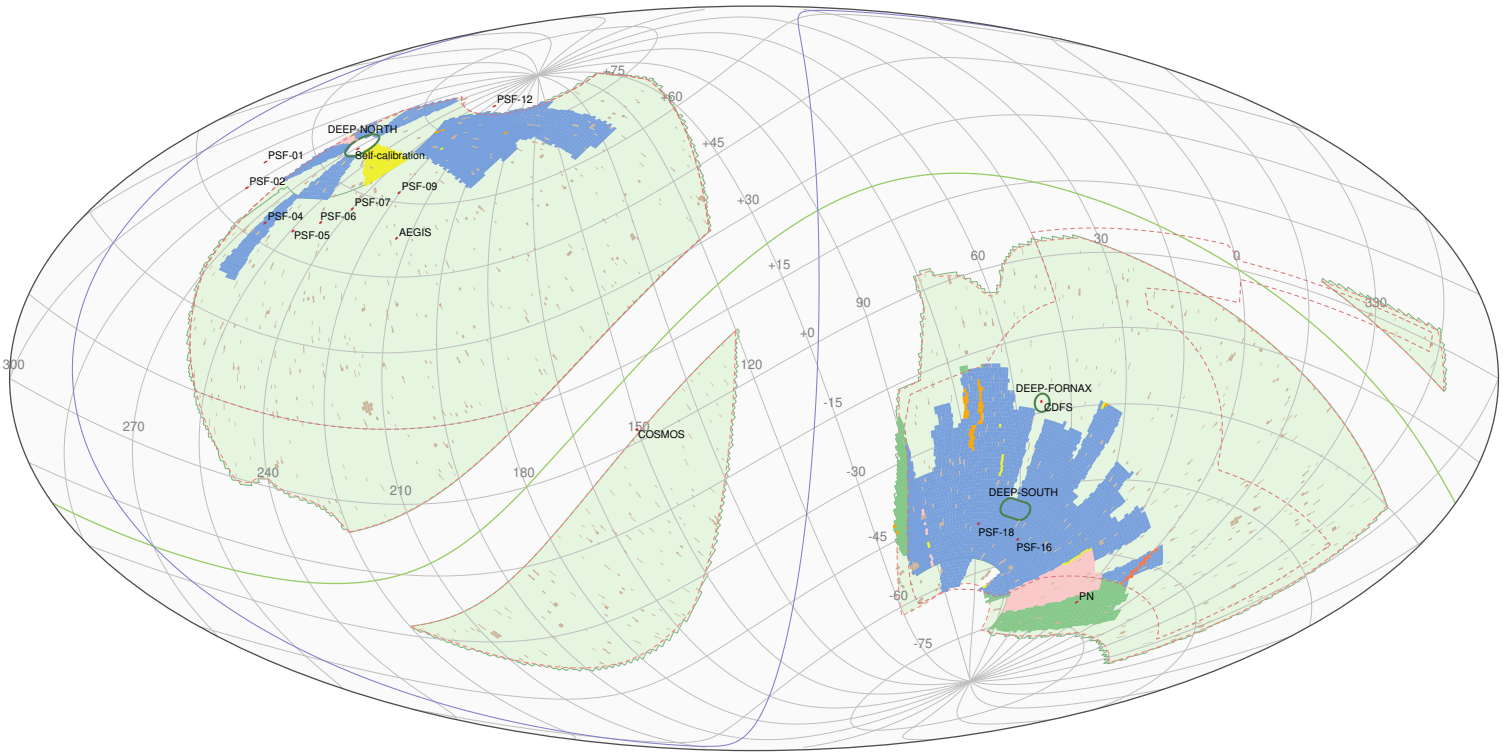


Fig. 6. The *Euclid* RSD Surveys at DR1, in the equatorial frame rotated around the central point (RA = 120°, Dec = 0°) to improve visibility of the polar regions. The EWS footprint (see Sect. 3.2) is shown in blue. The other colours show the EWS observations that were excluded from DR1: the red stripe of tiles in the south is the RA = 0 h region, pink patches show invalid ice-age observations not yet re-observed, orange tiles correspond to instrument outages and lack VIS data, yellow regions were scheduled and not executed, and green areas have no ground-based data (see text for details). Brown areas scattered on the map are the bright star exclusion regions. The RSD targets (see Sect. 3.3) included in DR1, i.e., the observed EDFs, EAFs, and all calibration fields (Self-calibration, planetary nebula and PSF fields) are also shown in the map. Dashed red countours mark the UNIONS (in the North) and DES (in the South) footprints where ground-based data are available. The orange line shows the ecliptic and the blue line the Galactic plane. The light green background shows the *Euclid* RoI, consisting of two mainlands and two islands, where the spacecraft continues its surveying mission.

Table 1. Summary properties of the DR1 Euclid Deep and Auxiliary Fields.

Type	Field	RA	Dec	Area design [deg^2]	No. Visits	Area 1 pass [deg^2]
EDS	EDF-N	269.°733	66.°02	20.0	11/40 (8R,3B)	30.6
	EDF-S	61.°241	−48.°42	22.7	10/45 (10R,0B)	33.0
	EDF-F	52.°932	−28.°09	10.0	2/52 (1R,1B)	13.2
EAF	COSMOS	150.°120	2.°21	2.0	27/75	2.6
	CDFS	53.°118	−27.°81	0.5	34/34	0.8
	AEGIS	214.°827	52.°82	1.0	18/18	1.4

Notes. Columns give the coordinates of the centres, the designed areas where the full depth will eventually be reached, the number of visits in DR1 as a fraction of the final number of visits planned (also showing the breakdown in ROS and ROS-Blue visits for the EDFs), and the area covered by at least one dither in DR1.

also note that a fraction of the EDF data was already released in Q1 (Euclid Collaboration: Aussel et al. 2026a). Indeed, Q1 consisted of one visit to each of the three EDFs, totalling 63.1 deg^2, plus data from the LDN 1641 field (see Sect. 5.2), with dozens of papers already published using that data set. The location and shape of the three EDFs are included in the all-sky map of Fig. 6.

Euclid makes repeated observations of six EAFs throughout the mission (Euclid Collaboration: Mellier et al. 2025), eventually reaching a depth of 5 times that of the EWS average. The data are used to calibrate photometric redshifts and to quantify the impact of colour gradients on shape measurement in the presence of a chromatic PSF. The observing strategy is to make repeated passes to the full area of these fields, increasing depth (each pass applies small shifts in the pointings). The passes alternate between the ROS and ROS-Blue sequences. DR1 includes data from three of these fields, as shown in Table 1. Again, the number of visits reported is the number of passes over the full fields, each corresponding to multiple obsIDs.

Only three of the EAFs are included in DR1, as shown in the all-sky map of Fig. 6. The visits to CDFS and AEGIS are al-

Table 2. Summary properties of the DR1 RSD calibration fields, grouped in three types.

Type	Field	RA	Dec	Area design [deg^2]	CALBLOCK	No. ObsIDs	Area 1 pass [deg^2]	Sequence
EUDF	SelfCal-centre	268.°813	65.°29	2.0	F-001	11	2.3	ROS-D1
					F-009	2		NISP (special)
					F-010	5		NISP (special)
					F-011	1		NISP (special)
					F-016	2		VIS (special)
					F-018	1		NISP (special)
	SelfCal-faint	268.°000	65.°00		F-007	10		VIS (special)
PN	SMC-SMP-20	14.°035	−70.°30	0.5	F-010	5	2.2	NISP (special)
					F-010	1		ROS
PSF	PSF-01	292.°48	53.°53	0.5	F-008	1	0.7	VIS (special)
					F-013	1		ROS
					F-015	1		VIS (special)
	PSF-02	285.°03	49.°83	0.5	F-008	2		VIS (special)
	PSF-04	265.°72	48.°09	0.5	F-008	1		VIS (special)
	PSF-05	254.°20	49.°37	0.5	F-008	1		VIS (special)
	PSF-06	247.°27	52.°69	0.5	F-008	1		VIS (special)
	PSF-07	239.°80	56.°89	0.5	F-008	1		VIS (special)
	PSF-09	225.°35	61.°91	0.5	F-008	1		VIS (special)
	PSF-012	218.°16	82.°06	0.5	F-008	1		VIS (special)
	PSF-016	59.°25	−55.°16	0.5	F-008	1		VIS (special)
	PSF-018	73.°52	−49.°10	0.5	F-008	1		VIS (special)

Notes. Columns give the coordinates of the centres, the designed areas, the larger area covered by at least one dither in DR1, the CALBLOCKS that contribute to each field, and the number of obsIDs and sequences executed. The Self-calibration field (in its two offset centres) gets most of the visits. The PSF fields are observed in three CALBLOCKS, as indicated for PSF-01.

ready completed in DR1. Each of these two fields was observed in two periods, separated by 6 months, implying that half of the passes share a common direction that is 180.°0-rotated with respect to the position angle of the second half of the visits. The third field, COSMOS, is the largest one and is 36 % complete in depth. Additional data on COSMOS and CDFS were taken in the PV phase and are also included in DR1 (see Sect. 5.2).

Observations to acquire data for calibrations define another set of fields in DR1, observed with a variety of observing sequences, as shown in Table 2. We point out that the various special sequences listed are different from each other, with a broad range of exposure times, and some including off-sky observations.

Several CALBLOCKS are executed in the Self-calibration field, with a diversity of observing sequences, most notably the 11 ROS-D1 observations made as part of the monthly F-001 self-calibration. The monthly F-007 VIS nonlinearity calibration is also executed in the same field, slightly offset to a region with a lower density of stars. Moreover, the Self-calibration field is contained in EDF-N and it was also a frequent target used in the PV phase (see Sect. 5.2). All these observations will contribute to form the deepest *Euclid* field, named the Euclid Ultra-Deep Field (EUDF), as mentioned in Euclid Collaboration: Mellier et al. (2025).

The single visit to the planetary nebula (PN) in the Small Magellanic Cloud (SMC) has a complex sequence, with a total of 456 pointings, most only in NISP, also including four ROS observations with the PN placed near the four corners of the FoV, which is responsible for the larger one-pass area reported in Table 2. The RSD visit is its second one, having also been observed during the PV phase (see Sect. 5.2).

The remaining calibration fields included in DR1 are 10 of the set of 24 fields defined for PSF calibration observations, with one of the fields, PSF-02, being used twice. Visits to PSF fields include the main CALBLOCK-F-008 VIS sequence, with 100 pointings, and also the CALBLOCK-F-013 single ROS observation as well as a short CALBLOCK-F-015 sequence. The observations are preceded by the CALBLOCK-F-012 closed shutter sequence. The sequence of three CALBLOCKS is executed for all these fields, although Table 2 only shows it for one field for the sake of brevity. We note that PSF-16 also contains data from the PDC campaign (see Sect. 6.1.1).

The DR1 RSD calibration fields, i.e., Self-calibration, SMC-SMP-20 (PN), and the 10 PSF fields, are included in the all-sky map of Fig. 6. PSF-01 and PSF-02 are outside the RoI, and hence are not covered by a ROS EWS tile. A dedicated ROS observation was scheduled on those fields, but not on time for DR1. PSF-12, at a high declination, is outside the reach of ground-based telescopes and was later removed from the set of PSF fields. All the DR1 RSD target fields are also represented in the full DR1 *Euclid* surveys map shown in Sect. 7.

Figure 7 shows three exposure maps containing the number of single-exposures at pixel level, resulting from the DR1 RSD observations. The figures highlight features of the EDFs, EAFs, and Self-calibration field, and provide a comparison between VIS and NISP exposures. The maps shown are the VIS EDF-S, the NISP COSMOS, and the VIS Self-calibration field.

The exposure map of EDF-S contains 10 ROS visits (see Table 1), hence each pointing is covered by 40 dithers. The number of exposures goes up to 48 in some pixels due to tile overlap, with a median of 33. The coverage is very homogeneous, with half of the pixels having between 31.5 and 34.5 exposures, and none with less than 20 exposures. Due to the execution of ob-

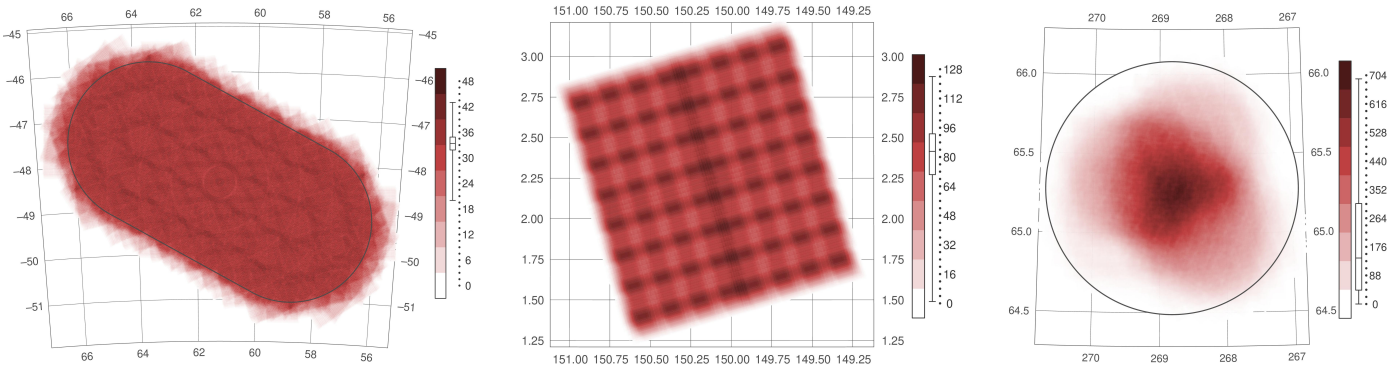


Fig. 7. Exposure maps showing the pixel coverage of EDF-S (in VIS; *left panel*), COSMOS (in NISP; *central panel*), and the Self-calibration field (in VIS; *right panel*). The scale includes a quartile bar, with the lower tick showing the first quartile (the median of the lower half of the exposure values), the middle tick showing the second quartile (the median of the full set of values), and the upper tick showing the third quartile (the median of the upper half of the exposure values). The box within the bar shows the inter-quartile range, i.e., the spread of the middle half of the points.

servations from various directions, circular patterns form in the map.

The exposure map of COSMOS corresponds to 27 ROS visits (see Table 1), hence to 108 exposures. The number of exposures goes up to 122, with a median of 85. The coverage is less homogeneous than in the EDF-S case, with a much larger spread in values. This happens because all visits are made in a single direction (and in the opposite 180° rotated direction), with small offsets applied to the pointings. The distribution of counts is not symmetric around the peak, with an excess of pixels on the lower side. The pattern formed by the contrast between high and low counts has an orthogonal shape, following the layout of the detector gaps, and is not circularised by multiple directions as in the EDF-S case. In general, the patterns are more noticeable in NISP than in VIS maps due to their different layout of gaps.

The exposure map of the Self-Calibration field corresponds to the 11 F-001 visits (see Table 2), with each visit containing 76 ROS-D1 pointings, there is a total of 836 exposures. The visits are made at a roughly monthly cadence, thus with different directions resulting in a roughly circular footprint of 2.0 deg^2, deeper in the centre. The applied offsets ensure a more homogeneous coverage of the central region without reaching the maximum possible number of exposures at the central point. We note that the Self-calibration field does not include the other calibration observations made in the same field with special observing sequences, nor the ones centred in SelfCal-faint nor the overlapping EDF-N visits.

Appendix A provides the complete set of VIS and NISP exposure maps for all EDFs, EAFs, and Self-calibration (only CALBLOCK-F-001) DR1 observations. It also contains the exposure maps of the PN field observations, and the VIS exposure map of the PSF-18 observations, which is representative of all other PSF fields.

4. Operational survey

The production of the *Euclid* survey does not end with the computation of the RSD and related files and documentation. Upon receiving an RSD, the *Euclid* SOC verifies its scientific validation and reports its conclusions in the RSD ingestion and analysis report (RIAR), proceeding then with its operational validation using Euclid survey system (ESS) tools. Afterwards, the SOC processes the RSD for operational use generating the OSS. This procedure involves a second input besides the RSD, namely the Instrument Commanding Requests (ICRs) provided by the Instrument Operation Team (IOT). Finally, the SOC generates the operational products to be transmitted to the MOC that operates the spacecraft.

A brief mention of the two ESS tools is appropriate. The Euclid Survey System Planning Tool (`ESSPT`; Gómez-Alvarez et al. 2018), based on the *Herschel* mission planning infrastructure, significantly extended and adapted for the *Euclid* mission, is a standalone Java tool. It loads an RSD and populates tables listing all patches (ID, observing dates, coordinates, and solar angles), and pointings. It contains a sky panel, showing the time-indexed survey patches in various coordinate frames and sky projections, with the possibility of drawing contours and overlaying maps and catalogues. It also produces survey statistics and verifies the survey compliance with the system requirements.

`ESSPT` could also be used to generate the full EWS, as an alternative to `ECTile`. For this, the user manually draws a patch on the sky panel, and the tool automatically schedules the patch with ROS pointings. The patch is then filled by tiles, starting from the bottom-right corner and progressing up and down in a zigzag way, with user inserting the time of the first pointing or, alternatively, its SAA. However, the manual patch placement procedure and the lack of integration with the other aspects of the complex scheduling (such as the implementation of the calibration plan), makes it unpractical to use `ESSPT` to produce the RSD, and the tool is mainly used for survey visualisation and characterisation.

The second ESS tool, the Euclid Survey System Operational Tool (`ESSOT`), is the one used by the SOC to process the RSD. It comprises all the functionalities of `ESSPT` plus the functionalities needed to generate the OSS, and the functionalities required to maintain the survey implementation throughout the mission. These include the following.

- OSS generation (Sect. 4.1).
- Operational products generation (Sect. 4.2).
- Operational reporting: automated report generation of the status of the survey; quick look analysis (QLA) ingestion to visualise the temporal and spatial evolution of selected values; and data volume and consumables estimation.
- Mission replanning (Sect. 4.3): the planning can be modified by removing current observations or importing new ones.

4.1. OSS generation

While the RSD provides a high-level description of the observations to be performed, the OSS contains the detailed implemen-

tation required for their execution. The OSS therefore represents the operational implementation of the survey.

The OSS is generated by the SOC using the ESSOT. Following validation of the RSD, the tool processes the RSD schedule and generates the corresponding OSS. This is done with two mechanisms applicable according to the type of observation sequence. In the case of ROS observations scheduled in the RSD, the detailed implementation is derived through the ROS processing performed by ESSOT, which populates the OSS XML file with the relevant ROS information, such as the grism and filter to be actuated in each frame.

In the case of calibration activities, the detailed implementation is made by inserting the references of the corresponding ICRs in the OSS. An ICR is the mechanism by which the VIS and NISP IOTs specify sequences of instrument commands not covered by the RSD. This mechanism is mainly used to specify the detailed calibration activities and consists of an XML file generated from two inputs produced by the IOT. The first input is an instruction file containing lists of target and dithering instructions; incidentally this information can be automatically retrieved from the CalF. The second input are CSV configuration files containing instrument operations instructions, structured as a script with the possibility to loop over blocks of instructions. There is one configuration file per CALBLOCK, containing the telecommand (as defined by MOC, based on the true instrument commands), the parameters defining the details of the telecommand, and the execution timing of the telecommand per pointing. Each pointing has a maximum window of 3000 s, which is the maximum duration the spacecraft can hold telecommunication contact with the ground station while holding a fixed pointing.

The OSS file incorporates the activities generated by the ESSOT for ROS observations, together with the applicable ICRs. Each new release of an OSS includes all the activities already executed and the future planned ones up to the nominal end of the mission.

4.2. Operational products generation

The SOC produces two operational products that are delivered to MOC at each planning cycle (PC). The operational planning products are generated for a specific PC. Each PC corresponds to the interval between two consecutive SOPS windows. The corresponding planning products are delivered by the SOC to the MOC at least 2 weeks before their on-board execution period.

The first operational product is the set of Survey Schedule Requests (SSRs) to be delivered to MOC flight dynamics (in the form of the SSR_FD file). The SSR_FD file is generated by the ESSOT, derived from the OSS, and contains the slew timeline together with the pointing information defining the spacecraft attitude for a given PC. An SSR_DEBUG file containing additional diagnostic information is also generated for internal SOC use to support validation of the SSR_FD generation process.

ESSOT also generates the ESS_EVENT file, which is intended for internal use within the SOC. This file contains the detailed implementation of ROS observations translated into SOC events, and also includes the implementation of calibration activities defined through ICRs. We note that, depending on the complexity of the activity, the calibrations may be represented either as SOC events or directly as telecommand sequences.

The ESS_EVENT file, together with the ICRs and the Mission Information Base is used as input to another set of tools, the SOC Commanding System (SCS) which is the system in charge of centralising and generating the commanding requests from the SOC, merging ESS and IOT requests. The SCS interprets the events and converts them into telecommand sequences according to a set of SOC-defined rules based on the Mission Information Base definitions, incorporating ICR-specific information when required. The SCS also assigns the corresponding parameter values to the generated telecommand sequences. The resulting output is encoded in the Payload Operation Request (POR) XML format, a file used to schedule and automate telecommands. This output file is packaged together with the PC delivery manifest, forming the so-called Command Request File Group (CRFG) product, which is the second operational product delivered to the MOC at each PC.

4.3. SOC survey replanning

Section 2.5 described strategic survey replanning implemented at the SOST level. However, sometimes there is the need for a quick localised modification of the survey plan while in operations, such as a one-off change that needs to be performed quickly, sacrificing temporarily a small part of the scheduled survey. These requests are studied and approved by the configuration control board (CCB) and a corresponding ICR is issued. Such modifications do not require a full-scale strategic replanning and are implemented by the SOC with one of two procedures:

- fast replanning, known as the palaeolithic approach;
- local optimised replanning, known as the neolithic approach.

In the palaeolithic approach, the change request is directly implemented. For example a new list of calibration pointings is requested to be observed at a given point in time, replacing the scheduled observations. This results in spatial and time gaps in the survey and no attempt is made to fill them. In cases where the ICR specifies earliest and latest start times (i.e., it includes a temporal margin), some level of performance optimisation is applied by introducing the modification in a least-damaging period. For this purpose, the ESSOT provides tools to find the worst figure of merit (FoM) within the ICR time window to guide the user selection. The spatial gaps introduced in this approach should be recovered at a later time, through a strategic replanning of the survey. This was the procedure followed to schedule the two decontamination campaigns. In the first campaign, the ICRs had a time margin that allowed us to implement the decontamination activities in replacement of calibrations that did not need to be rescheduled. In the second decontamination the ICR timings were stricter and the removed observations were later scheduled in a new RSD.

In contrast, the neolithic approach performs a local optimised replanning of the replaced observations. It applies only to fixed-time ICRs. The FoM of the replaced observations is compared to their neighbours and worse-quality neighbours are replaced by the removed observations that are thus reinserted with shifted starting times.

5. PV phase

We turn now to the observations performed in the epoch before the start of the RSD execution, which were implemented by the SOC. A large part of these observations contribute to the DR1 data set, thus also being part of the *Euclid* surveys. The first period after launch was the spacecraft commissioning. Most commissioning activities were not scheduled through standard SOC

tools and lack metadata. They are therefore considered incomplete and are not included in DR1. Following spacecraft commissioning, in early August 2023, the PV activities of technical characterisation and calibrations started, with a two-month plan of observations. Due to issues with the fine-guidance sensor (FGS; Laureijs et al. 2024), the PV phase was paused at the end of August 2023. It resumed a few days later, with tasks that did not require high pointing stability. At the end of September 2023, the FGS was recommissioned and PV activities restarted for an additional 2-month period until early December 2023. The full PV schedule is given in Euclid Collaboration: Schirmer et al. (2026a). It consists of 31 blocks of activities referenced as CALBLOCK-PV-XXX, and one labelled CALBLOCK-F-014, of which 11 fulfil VIS and NISP calibration products (PV-001 through PV-009, PV-035 and F-014), eight are tuned for NISP calibration products (PV-010 through PV-019), and 12 for VIS (PV-021 through PV-034). Three of the blocks are observed with ROS (PV-005, PV-007, F-014), six with ROS-D1 (PV-001, 003, 004, 006, 023, and 035), and the remaining implement special observing sequences using only one or both instruments.

5.1. PV phase implementation

Long before launch, a PV plan started to be prepared in the form of a document associated with a timeline built using the `Excel` software. This plan was used in feasibility studies concerned with the total PV duration and the daily downlink volume, among other parameters. Already before launch, the procedure was changed to a fully electronic system that used the actual SOC planning products in a feedback loop to the PV planning process.

The mechanism to construct the PV phase timeline is based on ICRs. Each calibration block is defined by the on-sky pointings and instrument commands, which constitute the required inputs to the SOC planning tools. The pointings are generated at the SOC, while the instrument commands are provided by the two instrument teams through a dedicated interface based on CSV files. For simplicity, most calibration blocks are devoted to a single instrument, with a few exceptions that observe with the ROS. From these inputs, the SOC generates the ICRs with a tool written using the `LabVIEW` programming environment. One ICR, or group of ICRs, is generated for each of the PV execution blocks.

The next step is to build the PV plan, i.e., to order the calibration blocks on a common timeline. This is done by the `PV scheduler`, a tool also written using the `LabVIEW` environment that in addition also permits the exchange of observational conditions and targets. Building the PV plan is a highly constrained problem. The most stringent constraint is target visibility in cases where specific targets are required and limited visibility windows exist. We also needed to place fundamental calibrations early in the schedule, since their calibration products were required for the data processing of higher-level observations (wavelength calibrations are a notable example). An additional constraint comes from the interruptions every 28 days through the SOPS windows that were also needed during PV. Not only do they prevent the placement of long calibration blocks that should not be interrupted, but they create a thermal impact. In addition, there was the need for rescheduling either because of failed observations, missed targets, deficient data quality, or additional engineering observations. To ease their sequencing, calibration blocks were broken up into smaller functional and self-consistent subsets called 'variants'. 114 variants were created out of the 31 executed PV CALBLOCKS. These helped in dealing with rescheduling, multiple executions, interruptions by SOPS windows or by other calibration blocks. The `PV scheduler` could then combine variants to again form higher-level indivisible execution blocks. The final PV timeline contains 132 execution blocks.

The PV schedule is then fed into `ESSOT` that performs a time consistency and constraints check. After removal of inconsistencies and fine-tuning, the plan is fed into a `LabVIEW` visualisation tool. The complex procedure of PV scheduling requires a very flexible and accurate `PV scheduler`, and the recurrent preparation of a visual plan that allows communication of the updated PV scheduling status to all stakeholders. During the four months of PV, a total of ten sets of SOC planning products were produced in the form of SSR_FD files, operational products delivered to MOC flight dynamics for execution. In the end, the PV schedule as executed made the most efficient use of *Euclid* 's in-orbit time, with almost no unused time gaps.

5.2. PV fields

The PV phase includes a very diverse set of observations. Table 3 provides the list of fields that resulted from the valid executions of on-sky PV CALBLOCKS. In the table, the fields are grouped by types. The first type consists of the ERO. ERO, or CALBLOCK-PV-007, contains six science programmes, executed in 17 fields, prepared to demonstrate *Euclid* 's capabilities in advance of the main mission, and constitute a first set of PV science fields. These data, acquired in 24 hours using the ROS, led to the public release of the first *Euclid* images in November 2023, and to a series of papers. The details of the six programmes and their 17 fields can be found in Cuillandre et al. (2025) and references therein.

The second type includes the ECSURV-defined observations for survey validation (CALBLOCK-PV-005) and background model characterisation (CALBLOCK-PV-006). The goal of the former is to ensure early on that *Euclid* performs as expected, that the deep field locations are without problems, and that survey-like data volume can be processed on the ground. They consist of one visit, executed with the ROS, to some of the EAFs and EDFs prior to their visits scheduled in the RSD. The fields selected for this programme were CDFS, COSMOS, EDF-S, and two observations of EDF-N (one pass to the full field and one pass to the central 3×3 tiles). The observations for characterisation of the zodiacal background models provide data used to validate the zodiacal model that guided the original choice of the *Euclid* RoI (Maris et al. 2019, see also Euclid Collaboration: Trombetti et al in prep.). The observations consist of three sets of pointings scanning the ecliptic latitude at fixed values of SAA, executed with ROS-D1. We note that each scan, consisting of several pointings, has a single observation ID. In particular, there is a set of 22 pointings made with SAA = 90°.0, 13 pointings made with SAA = 95°.0, and 13 pointings made with SAA = 100°.0. An additional set of 6 pointings, across the Galactic plane at constant ecliptic latitude, was performed to estimate diffuse star light contribution. The location of the 54 pointings of the five sequences is shown in Fig. 8, and each one constitutes a *Euclid* PV field.

The third type of observations consists of four calibrator fields observations that contain the VIS/NISP-P (CALBLOCK-PV-002) and NISP-S (CALBLOCK-PV-003) absolute photometric standards, a LMC high-density stellar field for the VIS astrometric solution (CALBLOCK-PV-023) and a compact PN with strong emission lines for the NISP wavelength dispersion

Table 3. Summary properties of the PV fields, grouped by type.

Type	Field	RA	Dec	CALBLOCKS	No. ObsIDs
ERO	17 fields			PV-007	25
Characterisation	CDFS	53°.118	−27°.81	PV-005	1
	COSMOS	150°.120	2°.21	PV-005	1
	EDF-S	61°.241	−48°.42	PV-005	1
	EDF-N	269°.733	66°.02	PV-005	2
	Scan-90 (z1–z22)	270°.000 to 310°.159	66°.56 to −23°.51	PV-006	1
	Scan-95 (z23–z35)	244°.546 to 317°.293	80°.00 to −26°.85	PV-006	1
	Scan-100 (z35–z48)	279°.438 to 322°.841	81°.38 to −25°.22	PV-006	1
	Scan-Gal (s1–s6)	257°.104 to 98°.221	75°.71 to −57°.32	PV-006	1
Calibrator	WDJ175318+644502	268°.345	64°.76	PV-002	3
	GRW+70	204°.650	70°.28	PV-003	5
	VIS-AST-1	90°.000	−66°.50	PV-023	2
	SMC-SMP-20	14°.035	−70°.30	PV-009	5
Stray light	αLyr	279°.858	39°.50	PV-004	1
	HD 165 906	271°.109	64°.83	PV-004	1
	SL1	279°.390	64°.82	PV-035	1
	SL2	268°.810 to 314°.540	65°.29 to 48°.23	PV-035	7
	SL3	267°.977 to 9°.276	66°.61 to −78°.25	PV-035	7
	SL4	(268°.445)	(66°.10)	PV-035	1
	SL5	(314°.539)	(73°.42)	PV-035	1
EUDF	Selfcal-centre	268°.813	65°.29	PV-001, 009, 016, 017, 019, 027, 028, 034, F-014	26
	Selfcal-faint	268°.000	65°.00	PV-011, 012, 014, 018, 021, 022, 024, 026, 027, 028, 029, 030, 031, 034	60
	NEP	270°.000	66°.56	PV-008, 018, F-014	22
EBF	EBF-06	257°.790	19°.47	PV-028, 034	7
	EBF-08	43°.945	−17°.63	PV-022, 027, 028, 029, 034	10
	EBF-10	350°.268	1°.32	PV-022	1
	EBF-12	0°.251	−75°.21	PV-022, 029, 030, 031, 033	12
FGS	LDN 1641	85°.754	−8°.39	OTHER	4

Notes. Each field may be observed for multiple purposes in different CALBLOCKS. The number of obsIDs is also given. One obsID may consist of observations of one field or a sequence of fields, in which case the coordinate range of the sequence is given, or in some cases the median point is given (in parenthesis). Most of the observations are done with special observing sequences, while some use the ROS, or the single-dither ROS-D1. See text for details.

(CALBLOCK-PV-009) that will be re-observed in the RSD. Most of these observations are ROS-like.

The fourth type contains the fields defined to defined to characterize the various stray light (expected and parasitic). The internal stray light check observes bright stars with an ROS-D1 sequence (CALBLOCK-PV-004). The external stray light check (CALBLOCK-PV-035) was a later addition to the PV plan, following the discovery of strong stray light from the Sun when observing at the pre-originally planned solar attitude (Euclid Collaboration: Mellier et al. 2025). this was aimed at sampling the AA/SAA parameter space to identify a survey operational range where the stray light is suppressed to a minimum. Five sequences of pointings were executed: SL1, with 13 observations in the same position with different AA values; SL2 and SL3, each consisting of a sequence of seven pointings with different SAAs each executed with seven AA values; SL4, a sequence of 17 pointings each executed with two AA values; and SL5, a sequence of 88 single pointings. PV-035 defined 120 fields in total, which are shown in the full sky map of Fig. 8.

The fifth type are observations made close to the North ecliptic pole (NEP) in the Self-calibration field, and in some cases pointing off-centre to an area within the field with lower density of bright stars (SelfCal-faint). Some of the observations are done off-sky, some on-sky and some have a sequence of both. These repeated visits to the NEP area, together with the recurrent visits to the Self-calibration field in the RSD, will result in the EUDF. The EUDF is currently being built with a dedicated data processing pipeline with data from PV-001 and F-014 PV observations, and from F-001 RSD observations (McCracken et al in prep.).

From *Euclid*'s orbit, the NEP region can only be observed with SAA close to 90°. The set of Euclid Blank Fields (EBFs) was defined by looking for alternative regions with low density of bright stars. They were selected to have a minimal density of stars brighter than 12 mag, and located at lower ecliptic latitudes, hence observable with different values of SAA. Some instrument calibrations, including additional observations of CALBLOCKS also executed in Selfcal-faint, were performed in four of these fields. This set of fields, defining the sixth type of PV fields, was no longer used in the RSD due to FGS guiding problems in the sparse fields and was replaced by Selfcal-faint.

Finally, there are the observations introduced for specific purposes outside the PV scope. In order to distinguish these from the regular PV observations they were given a dedicated ID, labelled 'OTHER', already at the moment of scheduling. Most of

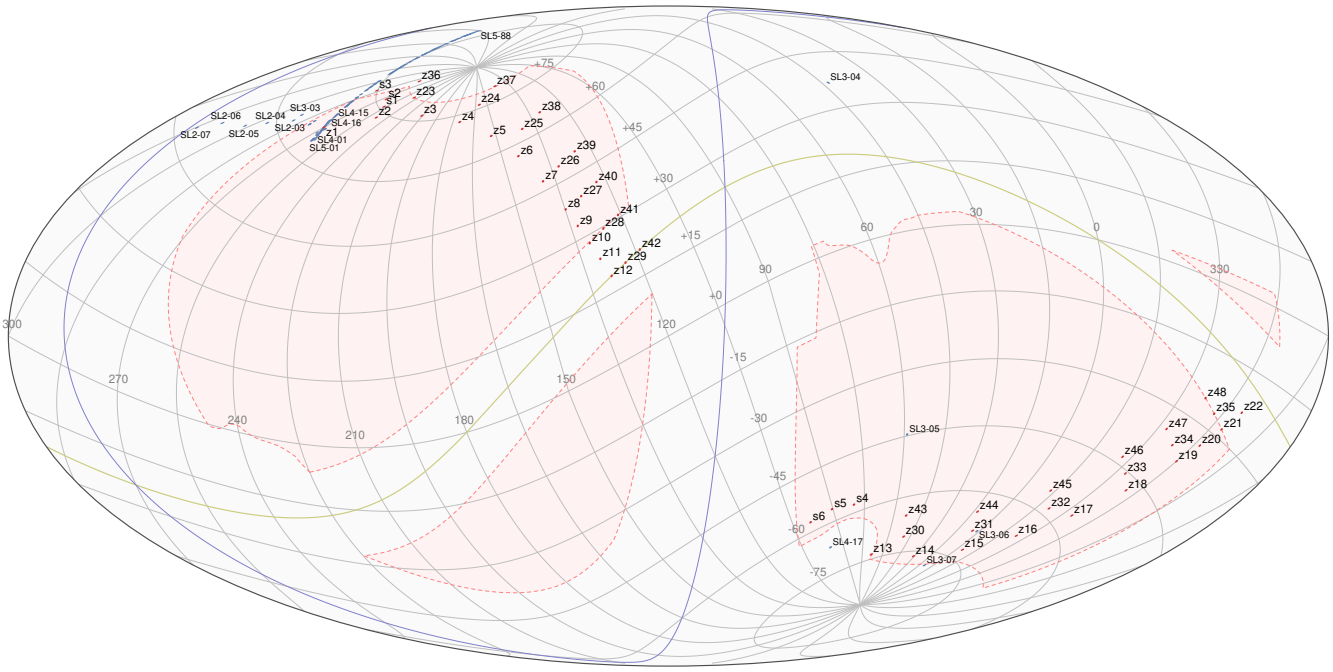


Fig. 8. The 174 fields observed in the ten PV-006 and PV-035 sequences, in a full-sky map in the equatorial frame rotated around the central point (RA = 120°, Dec = 0°) to improve the visibility of the polar regions. The orange line shows the ecliptic and the blue line the Galactic plane. The pink background shows the *Euclid* RoI. The 48 'z' pointings from PV-006 scan the ecliptic latitude in three sequences each with a constant SAA, while the six 's' pointings, also from PV-006, scan the Galactic latitude. The fields from the five PV-035 sequences are labelled SL1 through SL5. Most of them lie on the blue strip on the north, and are too crowded to label individually.

these special engineering observations are not included in DR1, with the exception of the dark cloud LDN1641, an extended dust-obscured part of the Orion A Cloud. This observation was made as part of the recommissioning of the FGS and ended up forming another PV science field. This field was already released as part of Q1 (Euclid Collaboration: Aussel et al. 2026a).

All these fields are part of DR1 as LE1 data. However, PV LE2 data cannot be obtained with the standard SGS processing. For this reason, the only PV fields present in LE2 data are the Self-calibration (PV-001 and F-014 observations only) and COSMOS (PV-005).

6. PDC campaign

The PV phase was followed by the PDC campaign. The rationale for this specialised calibration campaign is that the VIS PSF depends on the telescope optical path errors that vary with the thermo-elastic state of the spacecraft. In each pointing of the survey, the Sun illuminates the sunshield from a slightly different direction, primarily associated with variations in SAA and AA solar angles, producing a thermo-elastic variation of the spacecraft elements, including the position and shape of the telescope optical surfaces. In addition to the attitude of the spacecraft, the internal dissipation caused by the instrument cadence also greatly affects the thermo-elastic status of the telescope (Euclid Collaboration: Anselmi et al. 2026). These time-varying modulations result in a slightly different set of telescopes, where deviations from the reference fiducial telescope model translate into PSF variations. There is thus the need to perform observations with the aim of obtaining an accurate model of the in-orbit optical wavefront model of the telescope and its variation with the thermal state of the payload module. The procedure is performed by applying the so-called phase diversity technique, described in Euclid Collaboration: Schirmer et al. (2026a). The resulting wavefront error (Neumann et al. 2026) can be used to construct a basis set of models that may then be fitted to other data (Euclid Collaboration: Miller et al. in prep.).

6.1. PDC campaign implementation

The PDC campaign observation programme requires sampling of the space of spacecraft attitudes, and needs much more observations than those possible in the time allocated for the PV phase (where a first CALBLOCK-PV-008 phase-diversity test was performed). Indeed, the observing campaign lasted for about 70 days, until the start of the RSD execution on 14 February 2024.

6.1.1. PDC calibration fields

The observation plan of the PDC campaign consists of seven runs of observations, labelled PDC-2 through PDC-8, with a first run, PDC-1, previously executed during the PV phase on the NEP. Each run is performed in a different and fixed thermal state and focus conditions and with the instruments operated at a constant cadence. The requirement on thermal stability was defined as a less than 10-mK variation during out-of-focus observing sequences, and less than 60-mK variation for in-focus observations. In terms of solar attitude it was also verified that SAA variations have a greater thermal impact than AA variations, in agreement with Euclid Collaboration: Anselmi et al. (2026).

Within the stringent requirements of maximum SAA drift, four runs were implemented with sequences of out-of-focus VIS observations taking 3.2 days each, with the exception of PDC-5

Table 4. Summary properties of the PDC calibration fields.

Field	RA	Dec	Run	Duration [days]	Focus
NEP	270.°00	66.°56	PDC-2	3.2	out
			PDC-3	3.2	out
PSF-24	265.°07	71.°35	PDC-4	1.25	in
			PDC-5	3.2	out
Polarised	328.°00	70.°76	PDC-5	3.2	out
PSF-16	59.°25	−55.°16	PDC-6	3.2	out
PSF-10	221.°47	67.°43	PDC-7	1.25	in
PSF-23	87.°60	−47.°50	PDC-8	1.25	in

Notes. Run PDC-5 was the longest one, since it included observations of two low- and high-polarisation fields. The last column indicated if the observations were taken in-focus or out-of-focus.

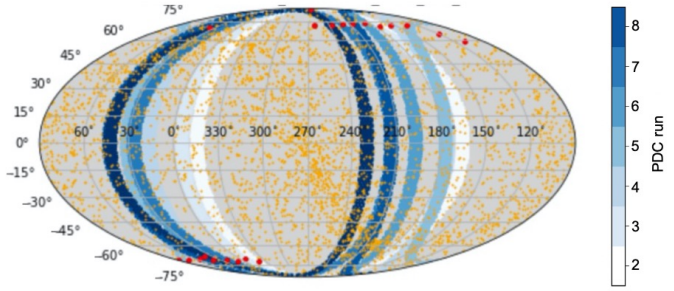


Fig. 9. Visibility windows for the seven runs of PDC-2 through PDC-8, on a full-sky map in the ecliptic frame. Each visibility window is shaped as a blue-shaded stripe 7° wide at the ecliptic and is computed for a specific value of the relevant input parameters (SAA, duration, and starting date). The set of PSF fields, potential targets for the calibration part of the run, are shown as red dots. Orange dots, which are distinctively denser in the Galactic plane, represent stars. The runs are designed to avoid pointing to bright stars in the stripes.

that contained two sets of observations, one in a low-polarisation and the other in a high-polarisation field. The remaining three runs implemented sequences of in-focus VIS observations of 1.25 days duration. The implementation was made by the SOC through the ICR mechanism. Whenever possible, the observations were made in the set of predefined PSF VIS fields used in the regular VIS PSF calibration observations during the EWS. An additional 'polarised' was defined, as well as a new PSF field at high ecliptic latitude (PSF-24) to ensure visibility to perform the tandem-sequences of PDC-5. NEP was used in PDC-2 and PDC-3 when no PSF field was visible. The PDC calibration fields used in this campaign are listed in Table 4.

6.1.2. PDC science fields

The stability in the thermal conditions required in the PDC campaign is much stricter than that used in standard EWS observations. It is thus necessary to allocate thermal stabilisation periods before each calibration run, where the spacecraft keeps its solar attitude fixed at the target SAA/AA value used in the subsequent calibration sequence. The first runs empirically confirmed the optimal duration of the thermal stabilisation period to be 7 days. The total thermalisation period is thus 50 days, accounting for 70 % of the duration of the PDC campaign.

The requirement of observing with a fixed attitude during 7 days with an imposed starting date, translates into the visibility windows shown in Fig. 9, one for each run. Those windows indicate that viable observing strategies must point along circles at a constant angle to the Sun. With the sky drifting roughly 1° per day, an ROS taking 1/20th of a day, and *Euclid*'s FoV being θ degrees wide depending on its orientation (with θ between 0.°7 and 1.°0), a contiguous survey can be obtained by returning to the same ecliptic latitude b after $20\,\theta\,/\,\cos b$ ROSs (with each new ROS stepping a full field along the meridian, to arrive at nominal EWS depth), or after $20\,\theta/(N\cos b)$ ROSs for N times the depth (by stepping $1/N$th of a field). In other words, the shorter the height of a patch of FoVs the larger the overlaps.

These constraints make it impractical to use the thermal stabilisation periods to start building the EWS, since the observations would be made in isolated patches difficult to connect later on with the EWS RSD progression. Moreover, the observations would be less efficient, with larger overlaps and heterogeneous depth. Alternative proposals that would benefit from the opportunity of taking multiple exposures in a confined region, adjusted to the natural drifting of the sky in the telescope frame, had to be considered.

The observations of the PDC science programmes were implemented by the SOC using a purpose-modified version of the `ESSOT` scheduling tool. In particular, a new patch-scheduling strategy was developed to automatically generate sequences of FoVs with large overlaps in user-defined patches. The FoVs are observed with the ROS and follow a time sequence that keeps SAA and AA constant during the 7-day run, defining a patch with height strongly correlated with its width and depth. Moreover, for the same height, patches at higher ecliptic latitudes have larger FoV overlaps. As mentioned before, shorter patches have larger FoV overlap, but this results in a heterogeneous depth across the patch, with varying coverage from the borders to the inner regions. This led to the introduction of a further constraint when defining the survey strategy, namely ensuring the coverage variation across a patch to remain below approximately 30In addition to developing this new patch-scheduling strategy, `ESSOT` also implemented a mechanism to avoid bright stars, and created a new feature of tilted patch geometry.

When executing the first run, PDC-2, a sudden drop of around 60 mK occurred in the base-plate temperature when starting the VIS calibration sequence. This was found to be caused by turning off NISP, that had been active in the thermalisation period for ROS observations of the first PDC science field. In the second run, PDC-3, ROS was again used in the first pointings of the thermalisation period, but was soon turned off in advance of the next calibration sequence. NISP was kept off during the thermalisation periods of all the subsequent runs that included out-of-focus observations. In result of this, the ROS was only used during the thermalisation periods that preceded the in-focus-only sequences, where the thermal constraints are weaker (runs PDC-4, 7, and 8). This measure had a significant impact on Euclid Medium-Deep Survey (EMDS) where only two of the five fields have NISP data.

The selection process of the PDC science fields is described in Sects. 6.2 to 6.4. Three scientific programmes were defined and executed: the EMDS; the ILS field; and the Euclid Ecliptic Survey (EES). The three programmes provided seven *Euclid* PDC science fields, with the EMDS comprising five of the fields. Table 5 summarizes the seven PDC science fields and their properties computed from the DR1 LE2 data. One pass is defined as one 4-dithered sequence, either ROS or VIS depending on the field, 1 ObsID corresponds to a 4-dithered sequence, and the depth is given in number of passes. The total area covered by at least 1 pass in VIS is 119 deg^2, while the total area covered by

Table 5. Summary properties of the seven PDC science fields.

Survey	Field	RA	Dec	Run	SAA	AA	No. ObsIDs	Depth median	Area 1 pass [deg^2]	Area 4 passes [deg^2]	Seq.
ILS	ILS-WAVES-S	355.°7	−31.°2	PDC-2	89.°7	−4.°5	135	1.5	26.5	0.0	ROS
EMDS	EMDS-WAVES-S	8.°2	−30.°7	PDC-3	90.°2	−6.°0	132	4.3	14.0	9.8	VIS
	EMDS-HSC-HL-1	208.°9	43.°5	PDC-5	97.°3	−3.°5	134	4.3	14.1	10.0	VIS
	EMDS-HSC-HL-2	237.°2	44.°2	PDC-6	87.°3	−3.°5	143	4.7	12.3	9.2	VIS
	EMDS-HSC-HL-3	214.°7	44.°3	PDC-7	107.°9	−4.°5	140	2.8	13.4	3.6	ROS
	EMDS-HSC-HL-4	230.°2	43.°6	PDC-8	101.°2	−4.°5	137	3.0	10.9	3.8	ROS
EES	SSO-ECLIPTIC	9.°8	4.°2	PDC-4	95.°9	−8.°0	149	3.5	16.8	4.5	ROS

Notes. Columns include the coordinates of the centres of the fields and the values of the solar angles fixed in the run. One pass is a 4-dithered sequence (either ROS or VIS-only, depending on the field), and corresponds to 1 obsID. The median number of passes across the field in the field's observing sequence, the area covered by 1 pass and the area covered by at least 4 passes, in the field's observing sequence, is also given, as well as the observing sequence.

at least 1 pass in NISP is a significantly lower 71 deg^2, leading to a total area of 68 deg^2 covered by at least 1 pass in ROS.

6.2. The Euclid Medium-Deep Survey

The Euclid Consortium's survey scientist at the time had since long advocated the usefulness of *Euclid* having an intermediate survey, 1 magnitude deeper and 1 order of magnitude smaller than the EWS. This idea from the start dubbed a 'medium deep survey' would fill the gap between the EDS and the EWS, since the former is 2 magnitudes deeper and over two orders of magnitude smaller than the latter. Such a survey would be achieved with six ROS visits (five additional visits to the one executed by the EWS) over an area of at least 500 deg^2.

The PDC thermalisation periods offered a unique opportunity to make repeated visits of the same area, and implement this long-standing proposal, in spite of not being sufficiently long to enable the coverage of the large area originally intended. It was thus a question of finding the right latitude and patch height to achieve the desired depth. On the other hand, the possible longitudes are constrained by the time of the observing runs, i.e., by the visibility windows of Fig. 9, which also implies that the survey cannot be contiguous but will need to be spread over separate fields.

An additional input to the problem of finding the optimal location for the EMDS fields is the fact that, as in the EWS, *Euclid* data need to be complemented with ground-based photometric data to be maximally useful. An extra requirement on the EMDS is therefore the presence of suitably deep multi-band surveys. This was largely achieved by leveraging the Hyper Suprime-Cam Subaru Strategic Programme (HSC-SSP) in the North (Aihara et al. 2018), and the Kilo-Degree Survey (KiDS-VIKING) in the South (de Jong et al. 2013). Both surveys add depth to the ground-based external data gathered for the EWS, and also form the basis for major spectroscopic surveys, with the Subaru Prime Focus Spectrograph (PFS) in the north (Takada et al. 2014) and the Wide Area VISTA Extragalactic Survey (WAVES) on the 4MOST spectroscopic facility in the south (Driver et al. 2019). Fortunately, these two surveys consist of long constant-declination strips on the sky, providing available fields at a wide range of ecliptic longitudes.

The EMDS programme was allocated in five of the runs, defining the five separate fields listed in Table 5, four overlapping the HSC-SSP high latitude area and one in the KiDS-VIKING region. Observations started in the south during the PDC-3 run, from 2023-12-13T10:19:22 to 2023-12-20T06:31:46, and then moved to the northern strip during runs PDC-5 to PCD-8, in the following observing epochs: 2024-01-02T00:18:02 to 2024-01-08T22:57:48; 2024-01-15T13:31:43 to 2024-01-22T06:02:13; 2024-01-26T00:45:01 to 2024-02-02T00:34:55; and 2024-02-03T11:52:19 to 2024-02-10T11:34:15.

The five EMDS fields are shown in Figs. 10 and 11, overlaid on the ground-based target areas. Their footprints show the individual VIS and NISP pointings computed with DR LE1 data. This choice highlights the difference between the LE1 and LE2 contents. For instance, EMDS-WAVES-S, the left field in Fig. 11, shows a number of NISP-only exposures on the edge of the field, that are not present in LE2 that only contains the ROS pointings for this field. These correspond to the first 13 pointings of the PDC-3 run that were still executed with NISP before being turned off.

The four EMDS-HSC fields, shown in Fig. 10 were named following the observing order, which does not follow an ordered sequence of longitudes due to the non-monotonic sequence of SAA values used in the runs. The fields observed in the two final runs, EMDS-HSC-HIGHLAT-3 and 4, are the only ones where NISP was turned on. Unfortunately, their 4-pass areas are significantly smaller than the 4-pass areas of the other EMDS fields. This happens for three reasons. On the one hand, the total overlap in exposures of two instruments is naturally smaller than the overlap of exposures of a single instrument. On the other hand, both runs experienced instrument outages that led to the loss of VIS data in around 25 obsIDs and NISP data in around 28 obsIDs in each run. In addition, these two fields are also the tallest ones, i.e, the most extended ones in ecliptic latitude. This implies that the resulting overlap between FoVs is smaller than in the shorter fields. This effect is striking in Fig. 11, which shows the two *Euclid* PDC WAVES-S fields, the EMDS and the ILS (see Sect. 6.3). The ILS field is a much taller patch, resulting in larger offsets and in a much smaller multiple exposed area.

In summary, the area with at least 4 times the depth of the EWS observed in both VIS and NISP in the EMDS only amounts to 7.3 deg^2 (see Table 5). In contrast, the total area of the EMDS covered with at least 4 passes in VIS is 43 deg^2, while the total area of the EMDS covered with at least 1 pass in VIS is 67 deg^2. Both depth and area are far from those originally proposed for an EMDS. At the moment, there are no defined plans for the continuation of this survey, except the fact that all five fields will be

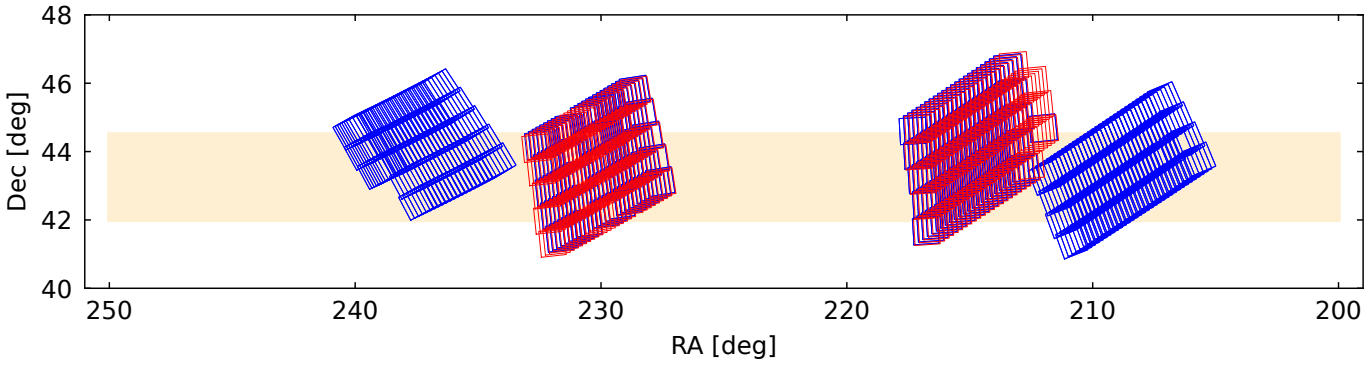


Fig. 10. Layout of the four EMDS fields in the northern sky. From left to right: EMDS-HSC-HIGHLAT-2; EMDS-HSC-HIGHLAT-4; EMDS-HSC-HIGHLAT-3; and EMDS-HSC-HIGHLAT-1. VIS exposures are plotted in blue and NIR exposures in red, with a small offset for clarity. The area with available HSC-SSP data is indicated in orange. Note that unlike for the EWS, there is considerable overlap between exposures, resulting in the over 4 times deeper exposure time in VIS.

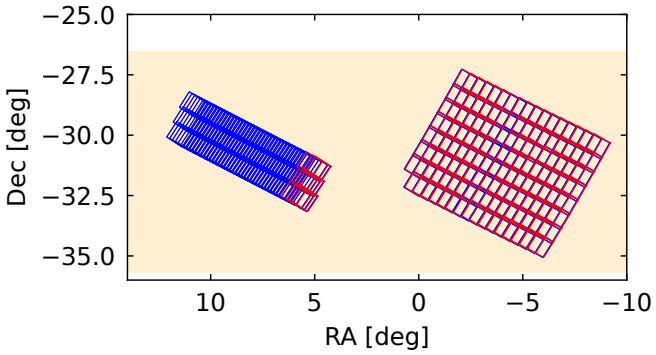


Fig. 11. Layout of EMDS-WAVES-S (left) and ILS-WAVES-S (right) in the southern sky at similar ecliptic latitude. The area with KiDS-VIKING data is indicated in orange. Note that the ILS field is a taller patch with larger offsets (50 % overlaps between tiles), resulting in an exposure time that is roughly double than that of the EWS, while the larger overlaps of the EMDS field result in a larger exposure time that is over 4 times that of the EWS.

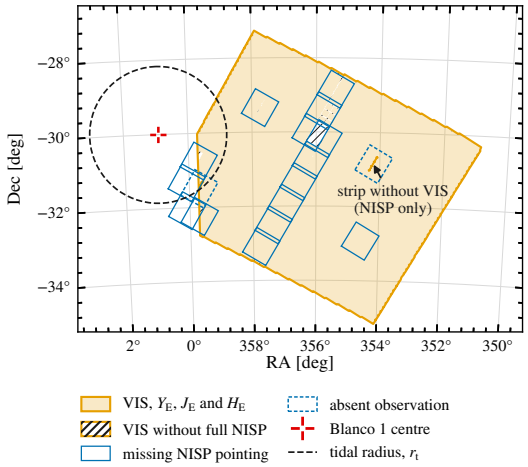


Fig. 12. ILS field covered in all *Euclid* bands except in the labelled areas. The field intersects the Blanco 1 open cluster tidal radius.

observed one more time as part of the EWS, some for DR2 and others for DR3, depending on future RSD replanning. Exposure maps of the seven PDC science fields, produced with DR1 LE2 data, are shown in Appendix A.

6.3. The ILS field

The two ILS scientists were granted a slot in thermalisation blocks 2 or 3 to propose a joint science programme. The field selection was made by consensus between the ILS scientists. Its properties were defined so that the field is part of the 4MOST/WAVES Wide South spectroscopic survey (Driver et al. 2019), which has previous *u*-, *g*-, *r*-, *i*-, *Z*-, *Y*-, *J*-, *H*-, and K_s-band imaging coverage by the VIKING (Edge et al. 2013) and KiDS surveys (de Jong et al. 2013; Wright et al. 2024) on VISTA and VST respectively, and that it should include members of a nearby young open cluster. The pre-existing, moderate-depth *Y*, *J*, and *H* imaging can be used for proper motions and a high density of redshifts will be obtained by the WAVES survey. The ILS programme aligned with the WAVES survey is primarily to study dwarf galaxies in the local cosmological volume using Euclid's imaging for detection and characterization of low-surface brightness galaxies. This is complemented by the WAVES Wide survey prioritization for obtaining spectra of galaxies at redshifts < 0.2. A second *Euclid* epoch is scheduled for DR3, when the field will be observed as part of the EWS.

The observations were performed from 2023-12-03T02:04:48 to 2023-12-10T02:22:58 in the PDC-2 run. The area covered by any number of exposures is 35.6 deg^2, the area covered by at least 1 ROS is 26.5 deg^2 (see Table 5), and the depth is 1–2 × ROS depth (1.5 for ROS and 1.75 for VIS-only exposures). The sequence of observations included 135 obsIDs, with two pointings missing in VIS, 16 in Y_E, 16 in J_E, and 15 in H_E, as shown in Fig. 12.

This programme managed to cover part of the nearby (distance 234 pc) Blanco 1 open cluster's corona and tidal tails and nothing of its core. Ten new comoving substellar-mass ultracool cluster member candidates have been identified using the *Euclid* photometry and spectra, and proper motions determined by comparison with ground-based imaging. These results extend the cluster sequence to cooler temperatures and fainter luminosities, build up on previous identifications of ultracool dwarfs based on ERO (Martín et al. 2025) and Q1 (Zerjal et al. 2026) data, and demonstrate the potential of *Euclid* to cover large area with deep observations that are crucial to reveal the very low mass population of nearby open clusters, particularly in the tidal tails.

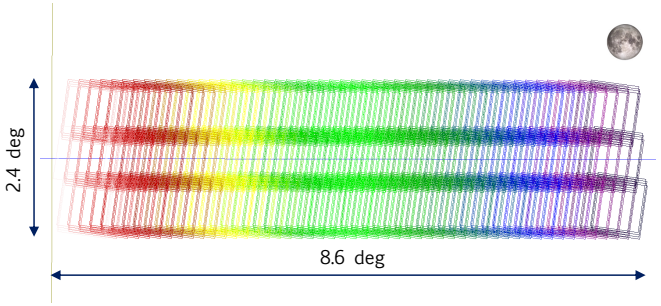


Fig. 13. Observing strategy of the EES, which starts on the rightmost squares on 23 December 2023 (black) and ends on the leftmost squares on 31 December 2023 (pink). The approximate centre point is on the ecliptic (horizontal line) at the ecliptic longitude of 10.°7. Each square corresponds to a single VIS exposure. Ecliptic longitude increases from right to left, and the ecliptic latitude increases from bottom to top (ecliptic north is up). The Moon is displayed for scale.

More observations of this cluster are needed for full coverage and proper motion studies of substellar candidate members.

6.4. The Euclid Ecliptic Survey

The remaining thermal stabilisation period was allocated to perform a survey on the ecliptic plane. The on-sky distribution of Solar System objects (SSOs) is heavily skewed towards the ecliptic plane. Based on the expected *Euclid* footprint, it has been estimated that about 150 000 SSOs would be observed during the EWS (Carry 2018). The estimate is, however, dependent on the actual size-frequency distributions of SSO populations and ecliptic latitude excursion of the survey. It was nevertheless clear that observing closer to the ecliptic plane would significantly increase the number of SSOs detected in each field. The *Euclid* Science Working Group SSOs therefore proposed a PDC survey focusing on the ecliptic plane.

The Euclid Ecliptic Survey, the PDC survey for SSOs, was designed to maximise the number of observations of SSOs, both in number of objects and in number of detections per object. During the campaign, from 2023-12-23T20:36:57 to 2023-12-31T14:18:20 in run PDC-4, the telescope was pointed at, or very close to, the ecliptic plane and approximately followed the average motion of objects in the main asteroid belt, thanks to the high overlap observing strategy implemented, which ensures that the asteroids are seen in as many exposures as possible (Fig. 13). This strategy allowed us to detect more SSOs and extract more astrometry over a longer timespan, as well as denser, longer rotational lightcurves, than would be possible in the EWS, which avoids the ecliptic plane and typically produces four detections of each moving target in its ROS observations. The total area covered by any exposure is about 19 deg^2, while roughly 17 deg^2 are covered by at least 1 ROS (see Table 5).

The outcome of the EES is presented in two papers. Pöntinen et al. (in prep.) presents the survey and the extraction of astrometry and photometry of about 4000 trailed moving objects (virtually all interior to Jupiter's orbit) from VIS exposures with tools developed for that particular task (Pöntinen et al. 2020) as well as NISP photometry for the same objects. The data allow us to test current knowledge on the orbit, size, and VIS/NISP taxonomic distributions beyond the completeness level reached by the other contemporary surveys. The other paper (Irureta-Goyena et al. 2026) describes extracted lightcurves from the streaks of 2321 known asteroids detected by Pöntinen et al. (in prep.), 93 % of which lack information about their rotation periods. Comparing to asteroids with rotation periods reported in the literature, they found that 98 % of the rotation periods extracted from EES agree to within 15 % of the rotation periods found in the literature. While the large majority of the asteroids analysed have rotation rates in agreement with the typical ranges for their physical size, there are also 16 superfast rotators with orbital periods shorter than the canonical 2.2 hour spin barrier.

7. Conclusions

We have presented the status of the *Euclid* surveys in the DR1 data release of 12 November 2026 (Euclid Collaboration: Aussel et al. 2026b). DR1 is the first major *Euclid* data release, following the Early Release Observation of 23 May 2024 (Cuillandre et al. 2025), consisting of PV-007 data, the Quick Data Release Q1 of 19 March 2025 (Euclid Collaboration: Aussel et al. 2026a), consisting of data from one visit to each of the EDFs and the LDN 1641 dark cloud, and the Quick Data Release Q2 of 24 June 2026 (Beaulieu et al. 2026), consisting of the Euclid Galactic Bulge Survey.

Euclid surveys refer to the various components of the overall programme that are executed during the three main phases of the mission, namely, the PV phase, the PDC campaign performed in the early science operations phase, and the much longer science operations phase, dubbed in this paper the RSD phase. The focus of this paper is on the survey implementation procedures applied in the three phases by both the Euclid Consortium and the SOC, as well as on the scheduling properties of the *Euclid* fields defined by the various survey components. The *Euclid* surveys are summarised in Fig. 14 and in Table 6. Figure 14 shows the location and extent of all *Euclid* fields included in the DR1 data release, while Table 6 provides a summary of the contents, epoch of observation, and scheduling procedure, of the *Euclid* surveys,

Acknowledgements. The Euclid Consortium acknowledges the European Space Agency and a number of agencies and institutes that have supported the development of *Euclid*, in particular the Agenzia Spaziale Italiana, the Austrian Forschungsförderungsgesellschaft funded through BMIMI, the Belgian Science Policy, the Canadian Euclid Consortium, the Deutsches Zentrum für Luft- und Raumfahrt, the DTU Space and the Niels Bohr Institute in Denmark, the French Centre National d'Etudes Spatiales, the Fundação para a Ciência e a Tecnologia, the Hungarian Academy of Sciences, the Ministerio de Ciencia, Innovación y Universidades, the National Aeronautics and Space Administration, the National Astronomical Observatory of Japan, the Netherlandse Onderzoekschool Voor Astronomie, the Norwegian Space Agency, the Research Council of Finland, the Romanian Space Agency, the Swiss Space Office (SSO) at the State Secretariat for Education, Research, and Innovation (SERI), and the United Kingdom Space Agency. A complete and detailed list is available on the *Euclid* web site (`www.euclid-ec.org/consortium/community/`). This work has made use of the *Euclid* Data Release 1 (DR1) from the European Space Agency (ESA) mission *Euclid*, available at `https://www.cosmos.esa.int/web/euclid/data-release-dr1`.

References

Abbott, T. M. C., Adamów, M., Aguena, M., et al. 2021, ApJS, 255, 20
Aihara, H., Arimoto, N., Armstrong, R., et al. 2018, PASJ, 70, S4
Beaulieu, J.-P., Bachelet, E., Gilles, M., et al. 2026, A&A, accepted, arXiv:2606.25883
Carry, B. 2018, A&A, 609, A113
Cuillandre, J.-C., Bertin, E., Bolzonella, M., et al. 2025, A&A, 697, A6
de Jong, J. T. A., Verdoes Kleijn, G. A., Kuijken, K. H., & Valentijn, E. A. 2013, Exp. Astron., 35, 25
Driver, S. P., Liske, J., Davies, L. J. M., et al. 2019, The Messenger, 175, 46
Edge, A., Sutherland, W., Kuijken, K., et al. 2013, The Messenger, 154, 32
Euclid Collaboration: Anselmi, A., Laureijs, R., Racca, G. D., et al. 2026, A&A, 709, A15

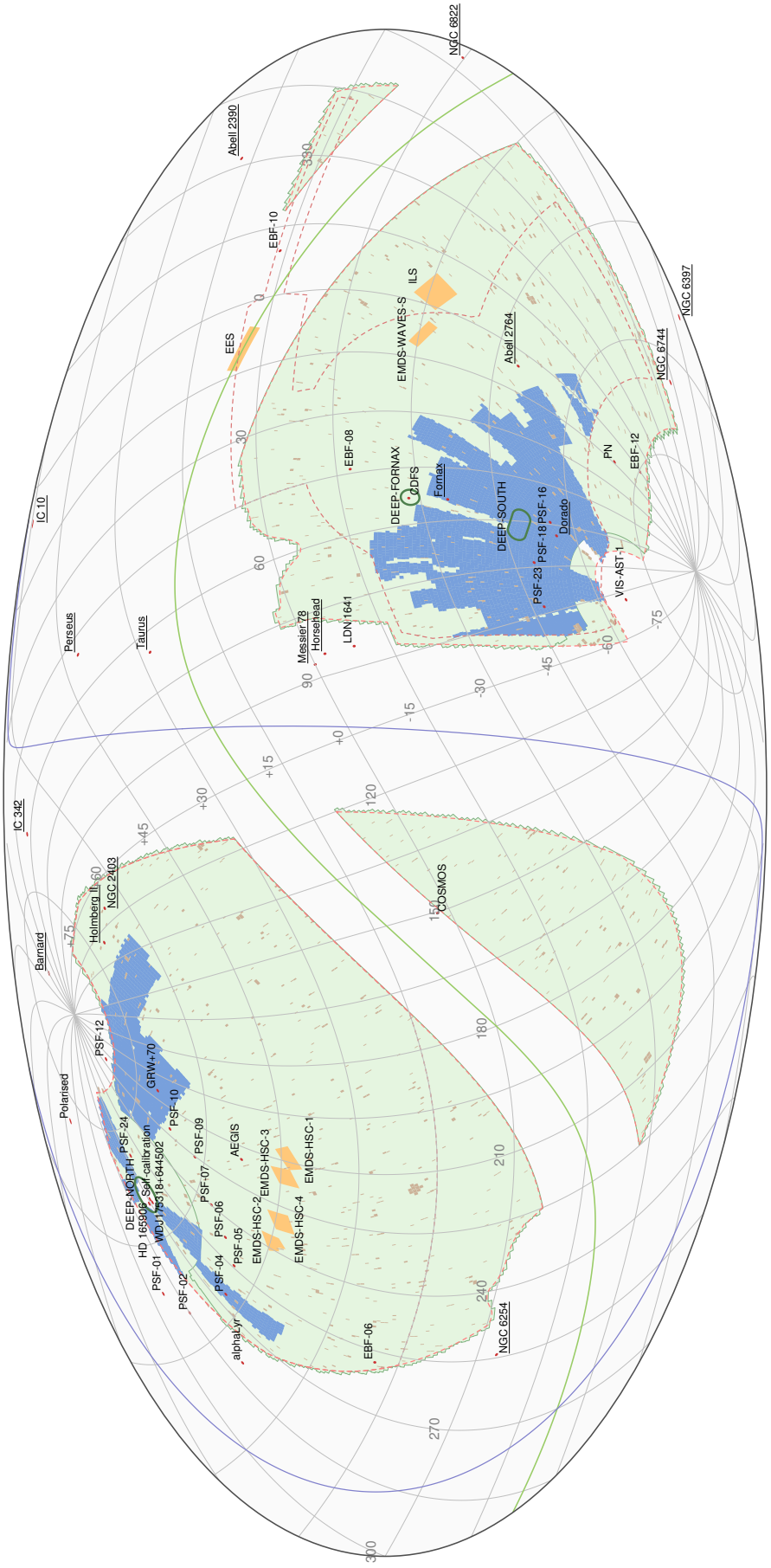


Fig. 14. The complete set of *Euclid* Surveys at DR1, with the exception of the 174 PV-006 and PV-035 fields to avoid cluttering the map (see Fig. 8), are shown in the equatorial frame rotated around the central point (RA = 120°, Dec = 0°) to improve visibility of the polar regions. The EWS footprint (Sect. 3.2) is shown in blue. The RSD targets (Sect. 3.3) included in DR1, i.e., the observed EDFs, EAFs, and calibration fields (Self-calibration, planetary nebula and PSF fields) are also represented in the map, as are the PV fields, including the 17 PV-007 ERO fields with underlined names (Sect. 5.2), the PDC calibration fields (Sect. 6.1.1) and the PDC surveys shown in orange (Sect. 6.1.2). Brown areas scattered on the map are the bright star exclusion regions. Dashed red countours mark the UNIONS (in the North) and DES (in the South) footprints where ground-based data are available. The orange line shows the ecliptic, and the blue line the Galactic plane. The light green background is the *Euclid* RoI, consisting of two mainlands and two islands, where the EWS continues its progress beyond DR1.

Table 6. The Euclid Surveys at DR1.

Survey component	Epoch	Contents	Procedure	Scheduled notes	Release notes
Wide survey	RSD	EWS tiles	`ECTile`	2639 deg^2	2099 deg^2 (LE1), 1900 deg^2 (LE2)
Deep survey	RSD	EDF-N, EDF-S, EDF-F	`ECTile`	7 EDF-N visits lost	28%, 22%, 4% of final depth
	PV	EDF-N, EDF-S	ICR		not included in LE2
Auxiliary fields	RSD	COSMOS, CDFS, AEGIS	`ECTile`		36%, 100%, 100% of final depth
	PV	COSMOS, CDFS	ICR		only COSMOS in LE2
Calibration fields	RSD	Self-calibration, PN, PSFs	`ECTile`		
	PV	Self-calibration, EBFs, calibrators, LDN1641	ICR		only PV-001 and F-014 in LE2 LDN also in Q1
	PDC	PSFs	ICR	defocus	
PV science fields	PV	PV-006, PV-007, SLs	ICR		not in LE2, PV-007 also in ERO
PDC surveys	PDC	EMDS	`ESSOT`		64.7 deg^2, of which 36.4 deg^2 with 4 passes
		ILS field, EES	`ESSOT`		26.5 deg^2, 16.8 deg^2

Notes. For each survey component, the table indicates the observation epochs, its fields, and the scheduling procedure applied. Information is given on the EWS area variation between RSD-scheduled, LE1, and LE2, as well as on the DR1 depths of the EDFs and EAFs. The ROS-observed areas of the PDC surveys are given and some release notes on the PV fields are included.

Euclid Collaboration: Aussel, H., Tereno, I., Schirmer, M., et al. 2026a, A&A, 711, A1
Euclid Collaboration: Aussel, H. et al. 2026b, arXiv, submitted
Euclid Collaboration: Corcho-Caballero, P., Balbinot, E., De Jong, J., et al. 2026, A&A, submitted
Euclid Collaboration: Cropper, M., Al-Bahlawan, A., Amiaux, J., et al. 2025, A&A, 697, A2
Euclid Collaboration: Hartley, W., Paltani, S., Dubath, F., et al. 2026, A&A, submitted
Euclid Collaboration: Jahnke, K., Gillard, W., Schirmer, M., et al. 2025, A&A, 697, A3
Euclid Collaboration: Kümmel, M., Caro, F., Dimauro, P., et al. 2026, A&A, submitted
Euclid Collaboration: Le Brun, V., Bethermin, M., Moresco, M., et al. 2026, A&A, submitted
Euclid Collaboration: McCracken, H., Benson, K., Cropper, M., et al. 2026, A&A, submitted
Euclid Collaboration: Mellier, Y., Abdurro'uf, Acevedo Barroso, J., et al. 2025, A&A, 697, A1
Euclid Collaboration: Polenta, G., Frailis, M., Alavi, A., et al. 2026, A&A, submitted
Euclid Collaboration: Ruffenach, M., Frailis, M., Zacchei, A., et al. 2026, A&A, submitted
Euclid Collaboration: Scaramella, R., Amiaux, J., Mellier, Y., et al. 2022, A&A, 662, A112
Euclid Collaboration: Schirmer, M., Paterson, K., Alavi, A., et al. 2026a, A&A, submitted
Euclid Collaboration: Schirmer, M., Paterson, K., Altieri, B., et al. 2026b, A&A, submitted
Euclid Collaboration: Schirmer, M., Thürmer, K., Bras, B., et al. 2023, A&A, 675, A142
Euclid Collaboration: Scodeggio, M., Copin, Y., et al. 2026, in preparation
Euclid Data Release 1. 2026, https://doi.org/10.57780/esa-d079c51
Gómez-Alvarez, P., Dupac, X., Buenadicha, G., et al. 2018, in SPIE Conf. Ser., Vol. 10707, Software and Cyberinfrastructure for Astronomy V, ed. J. C. Guzman & J. Ibsen, 1070712
Gwyn, S., McConnachie, A., Cuillandre, J.-C., et al. 2025, AJ, 170, 324
Irureta-Goyena, B. Y., Altieri, B., Kneib, J.-P., et al. 2026, A&A, 710, A27
Ivezić, Ž., Kahn, S. M., Tyson, J. A., et al. 2019, ApJ, 873, 111
Laureijs, R., Vavrek, R., Racca, G. D., et al. 2024, in SPIE Conf. Ser., Vol. 13092, Space Telescopes and Instrumentation 2024: Optical, Infrared, and Millimeter Wave, ed. L. E. Coyle, S. Matsuura, & M. D. Perrin, 130920M
Maris, M., Scaramella, R., Burigana, C., et al. 2019, in Astronomical Society of the Pacific Conference Series, Vol. 521, Astronomical Data Analysis Software and Systems XXVI, ed. M. Molinaro, K. Shortridge, & F. Pasian, 531
Martín, E. L., Žerjal, M., Bouy, H., et al. 2025, A&A, 697, A7
Neumann, D., Miller, L., Hoekstra, H., et al. 2026, A&A, accepted, arXiv:2606.25625
Pöntinen, M., Granvik, M., Nucita, A. A., et al. 2020, A&A, 644, A35
Takada, M., Ellis, R. S., Chiba, M., et al. 2014, PASJ, 66, R1
Wright, A. H., Kuijken, K., Hildebrandt, H., et al. 2024, A&A, 686, A170
Zerjal, M., Dominguez-Tagle, C., Vitas, N., et al. 2026, A&A, 711, A37

Authors and affiliations

Euclid Collaboration: I. Tereno[⋆1,2], J. Dinis[1,2], X. Dupac[3], R. Scaramella[4], B. Altieri[3], H. Aussel[5], I. Baldry[6], P. Battaglia[7], G. Buenadicha[3], C. Burigana[8,9], B. Carry[10], P. Casenove[11], J.-C. Cuillandre[5], C. Dominguez-Tagle[12,13], A. Franco[14,15,16], B. R. Granett[17], M. Granvik[18,19], A. Gregorio[20,21,22], B. Y. Irureta-Goyena[23], R. Kohley[3], K. Kuijken[24], P. Liebing[25], E. L. Martín[12,13], J. Martín-Fleitas[26], J. Mendes[27], L. Miller[28], A. A. Nucita[14,15,16], R. Nakajima[29], K. Paterson[30], V. Pettorino[31], M. Pöntinen[18], G. D. Racca[24,31], E. Romelli[21], M. Schirmer[30], M. Schmidt[27], T. Schrabback[32], D. Scott[33], C. Sirignano[34,35], R. Tata[36], T. Trombetti[8], A. Zacchei[21,37], M. Žerjal[12,13], S. Andreon[17], N. Auricchio[7], S. Awan[25], C. Baccigalupi[37,21,22,38], M. Baldi[39,7,40], A. Balestra[41], S. Bardelli[7], A. N. Belikov[42,43], R. Bender[44,45], A. Biviano[21,37], R. P. Blake[46], M. Bolzonella[7], A. Bonchi[47], E. Branchini[48,49,17], M. Brescia[50,51], J. Brinchmann[52,53,54], S. Camera[55,56,57], G. Cañas-Herrera[24], V. Capobianco[57], C. Carbone[58], V. F. Cardone[4,59], J. Carretero[60,61], R. Casas[62,63], F. J. Castander[63,62], M. Castellano[4], G. Castignani[7], S. Cavuoti[51,64], P.-Y. Chabaud[65], K. C. Chambers[66], A. Cimatti[67], C. Colodro-Conde[12], G. Congedo[46], C. J. Conselice[68], L. Conversi[69,3], Y. Copin[70], A. Costille[65], F. Courbin[71,72,73], H. M. Courtois[74], M. Cropper[25], A. Da Silva[1,2], H. Degaudenzi[75], S. de la Torre[65], G. De Lucia[21], H. Dole[76,77], F. Dubath[75], S. Escoffier[78], M. Farina[79], R. Farinelli[7], S. Farrens[5], F. Faustini[4], S. Ferriol[70], P. Fosalba[62,63], S. Fotopoulou[80], N. Fourmanoit[78], M. Frailis[21], E. Franceschi[7], M. Fumana[58], L. Gabarra[28], S. Galeotta[21], K. George[81], W. Gillard[78], C. Giocoli[7,40], J. Gracia-Carpio[44], A. Grazian[41], F. Grupp[44,45], L. Guzzo[82,17,83], W. G. Hartley[75], S. V. H. Haugan[84], G. Helou[85,86], S. Hemmati[86], H. Hoekstra[24], M. S. Holliman[46], W. Holmes[87], I. M. Hook[88], F. Hormuth[89], A. Hornstrup[90,91], K. Jahnke[30], M. Jhabvala[92], S. Kermiche[78], A. Kiessling[87], B. Kubik[70], M. Kümmel[45], M. Kunz[93], H. Kurki-Suonio[18,94], A. M. C. Le Brun[95], V. Le Brun[65], D. Le Mignant[65], S. Ligori[57], P. B. Lilje[84], V. Lindholm[18,94], I. Lloro[96], M. Maglioccheti[79], G. Mainetti[97], O. Marggraf[29], M. Martinelli[4,59], N. Martinet[65], F. Marulli[98,7,40], R. J. Massey[99], N. Mauri[67,40], S. Maurogordato[10], H. J. McCracken[100], C. J. R. McPartland[91,101], E. Medinaceli[7], S. Mei[102,103], M. Meneghetti[7,40], E. Merlin[41], G. Meylan[23], P. Monaco[20,21,22,37], M. Moresco[98,7], C. Moretti[21,37,22], L. Moscardini[98,7,40], E. Munari[21,37], C. Neissner[104,61], R. C. Nichol[105], S.-M. Niemi[31], C. Padilla[104], S. Paltani[75], F. Pasian[21], J. A. Peacock[46], W. J. Percival[106,107,108], S. Pires[5], G. Polenta[47], M. Poncet[11], L. A. Popa[109], L. Pozzetti[7], F. Raison[44], A. Refregier[110], A. Renzi[34,35,7], J. Rhodes[87], G. Riccio[51], I. Risso[48,49,17], H.-W. Rix[30], F. Rizzo[21], M. Roncarelli[7], C. Rosset[102], B. Rusholme[86], R. Saglia[45,44], Z. Sakr[111,112,113], A. G. Sánchez[44], D. Sapone[114], M. Sauvage[5], P. Schneider[29], M. Scodeggio[58], A. Secroun[78], E. Sefusatti[21,37,22], E. Sihvola[18,94], P. Simon[29], G. Sirri[40], A. Spurio Mancini[115], L. Stanco[35], P. Tallada-Crespí[60,61], A. N. Taylor[46], H. I. Teplitz[116], N. Tessore[25], S. Toft[117,101], R. Toledo-Moreo[118,119], F. Torradeflot[61,60], A. Tsyganov[120], I. Tutusaus[63,62,112], E. A. Valentijn[42], J. Valiviita[18,94], T. Vassallo[21,81], G. Verdoes Kleijn[42], A. Veropalumbo[17,49,48], D. Vibert[65], Y. Wang[86], J. Weller[45,44], G. Zamorani[7], F. M. Zerbi[17], E. Zucca[7], V. Allevato[51], I. T. Andika[45], M. Ballardini[121,122,7], P. Bergamini[7], S. Borgani[20,37,21,22,123], E. Bozzo[75], M. Calabrese[124,58], A. Cappi[10,7], F. Caro[4], T. Castro[125,21,37], S. Conseil[126,70], G. Daste[65], D. Di Ferdinando[40], J. A. Escartin Vigo[44], G. Fabbian[76], J. García-Bellido[111], T. Gasparetto[4], C. M. Gutierrez[12,13], A. Hall[46], Y. Kang[32], A. Loureiro[127,128], J. F. Macias-Perez[129], R. Maoli[130,4], R. B. Metcalf[98,7], S. Nadathur[131], L. Patrizii[40], E. Sarpa[21], V. Scottez[132,133], M. Sereno[7,40], K. Tanidis[134], M. Tenti[40], A. Troja[21], M. Tucci[75], M. Viel[37,21,38,22,123], J. R. Weaver[135], M. Wiesmann[84], Abdurro'uf[136], J. A. Acevedo Barroso[87], R. Adam[10], Y. Akrami[111,137], G. Alguero[129], G. Angora[51,121], S. Anselmi[35,34,138], M. Archidiacono[82,83], G. Aricò[40], F. Atrio-Barandela[139], M. Aubert[70], E. Aubourg[102,140], M. Baes[141], N. Bartolo[34,35,41], L. Bazzanini[8,121], J. R. Bermejo-Climent[142,143], D. Bertacca[34,41,35], M. Bethermin[144], F. Beutler[46], A. Blanchard[112], H. Böhringer[44,81,145], M. Bonici[106,58], F. Bouchè[146,64], M. L. Brown[68], S. Bruton[85], F. Buitrago[147,148,149], A. Calabro[4], P. Carrilho[150], C. S. Carvalho[149], N. Chartab[86], F. Cogato[7], T. E. Collett[131], T. Contini[112], P. Corcho-Caballero[42], M. Correnti[4,47], M. Costanzi[20,21,37], B. Csizi[32], O. Cucciati[7], H. Dannerbauer[12,13], T. de Boer[66], F. De Paolis[14,15,16], G. Desprez[42], A. Díaz-Sánchez[151], S. Di Domizio[48,49], J. M. Diego[152], P. Dimauro[153,4], P.-A. Duc[144], F. Dufresne[65], V. Duret[154], A. Eggemeier[29], A. Enia[155,7], Y. Fang[45], A. Farina[17,49], A. M. N. Ferguson[46], P. G. Ferreira[28], A. Finoguenov[18], A. Fontana[4], F. Fontanot[21,37], N. Frusciante[156,157], A. Fumagalli[21], Y. Fu[24,42], K. Ganga[102], R. Gavazzi[65,100], E. Gaztanaga[63,62,131], Z. Ghaffari[21,37], F. Giacomini[40], F. Gianotti[7], G. Gozaliasl[158,18], A. Gruppuso[7,40], M. Guidi[39,7], N. A. Hatch[159], C. Hernández-Monteagudo[13,12], T. Heuberger[160], H. Hildebrandt[161], J. Hjorth[162], M. Jauzac[163,99,164,165,112], S. Joudaki[60,131], J. J. E. Kajava[166,167,168], D. Karagiannis[169,121,170], J. Kim[28], C. C. Kirkpatrick[171], A. Kovács[143,142], I. Kovačić[141], K. Koyama[131], S. Kruk[3], M. C. Lam[46], M. Lattanzi[122], F. Leclercq[100], S. Lee[36,87], J. Le Graet[78], M. Lembo[100], M. D. Lepinzan[21], G. F. Lesci[8], J. Lesgourgues[172], T. I. Liaudat[140], L. Linke[32], A. Manjón-García[151], F. Mannucci[173], M. Marinucci[174], F. R. Marleau[32], C. J. A. P. Martins[175,53], M. Migliaccio[176,177], M. Miluzio[3,178], G. Morgante[7], C. Murray[5],

K. Naidoo[131,30], P. Natoli[121,122], A. Navarro-Alsina[29], A. Nersesian[179,141], S. Nesseris[111], L. Nicastro[7], M. Oguri[180,181], F. Oppizzi[49,35,34], F. Pace[55,56,57,2], M. J. Page[25], D. Paoletti[7,9], G. Papini[7,98], G. Parimbelli[63,38], F. Passalacqua[35], C. Pattison[131], A. Pisani[78], L. Pizzuti[182], J. J. Popp[183], D. Potter[184], M. Poulain[185], G. W. Pratt[5], S. Quai[98,7], M. Radovich[41], F. Ricci[186,4], G. Rodighiero[34,41], W. Roster[44], M. Sahlén[187], D. B. Sanders[66], C. Scarlata[188], J. Schaye[24], A. Schneider[184], D. Sciotti[4,59], E. Sellentin[189,24], S. Serjeant[183], F. Shankar[190], L. C. Smith[191], F. Soldano[100], S. A. Stanford[192], I. Szapudi[66], M. Talia[98,7], F. Tarsitano[193,110], G. Testera[49], R. Teyssier[194], S. Tosi[48,17,49], C. Uhlemann[195], M. Urbano[159,144], C. Valieri[40], A. Venhola[185], D. Vergani[7], G. Vernardos[196,197], A. Viitanen[75,171,4], E. Vilenius[25], S. Vinciguerra[65], M. von Wietersheim-Kramsta[99,163], N. A. Walton[191], L. Wang[198,42], and A. H. Wright[161]

[1] Departamento de Física, Faculdade de Ciências, Universidade de Lisboa, Edifício C8, Campo Grande, PT1749-016 Lisboa, Portugal
[2] Instituto de Astrofísica e Ciências do Espaço, Faculdade de Ciências, Universidade de Lisboa, Campo Grande, 1749-016 Lisboa, Portugal
[3] ESAC/ESA, Camino Bajo del Castillo, s/n., Urb. Villafranca del Castillo, 28692 Villanueva de la Cañada, Madrid, Spain
[4] INAF-Osservatorio Astronomico di Roma, Via Frascati 33, 00078 Monteporzio Catone, Italy
[5] Université Paris-Saclay, Université Paris Cité, CEA, CNRS, AIM, 91191, Gif-sur-Yvette, France
[6] Astrophysics Research Institute, Liverpool John Moores University, 146 Brownlow Hill, Liverpool L3 5RF, UK
[7] INAF-Osservatorio di Astrofisica e Scienza dello Spazio di Bologna, Via Piero Gobetti 93/3, 40129 Bologna, Italy
[8] INAF, Istituto di Radioastronomia, Via Piero Gobetti 101, 40129 Bologna, Italy
[9] INFN-Bologna, Via Irnerio 46, 40126 Bologna, Italy
[10] Université Côte d'Azur, Observatoire de la Côte d'Azur, CNRS, Laboratoire Lagrange, Bd de l'Observatoire, CS 34229, 06304 Nice cedex 4, France
[11] Centre National d'Etudes Spatiales – Centre spatial de Toulouse, 18 avenue Edouard Belin, 31401 Toulouse Cedex 9, France
[12] Instituto de Astrofísica de Canarias, E-38205 La Laguna, Tenerife, Spain
[13] Universidad de La Laguna, Dpto. Astrofísica, E-38206 La Laguna, Tenerife, Spain
[14] Department of Mathematics and Physics E. De Giorgi, University of Salento, Via per Arnesano, CP-I93, 73100, Lecce, Italy
[15] INFN, Sezione di Lecce, Via per Arnesano, CP-193, 73100, Lecce, Italy
[16] INAF-Sezione di Lecce, c/o Dipartimento Matematica e Fisica, Via per Arnesano, 73100, Lecce, Italy
[17] INAF-Osservatorio Astronomico di Brera, Via Brera 28, 20122 Milano, Italy
[18] Department of Physics, P.O. Box 64, University of Helsinki, 00014 Helsinki, Finland
[19] Asteroid Engineering Laboratory, Luleå University of Technology, Box 848, 98128 Kiruna, Sweden
[20] Dipartimento di Fisica - Sezione di Astronomia, Università di Trieste, Via Tiepolo 11, 34131 Trieste, Italy
[21] INAF-Osservatorio Astronomico di Trieste, Via G. B. Tiepolo 11, 34143 Trieste, Italy
[22] INFN, Sezione di Trieste, Via Valerio 2, 34127 Trieste TS, Italy
[23] Institute of Physics, Laboratory of Astrophysics, Ecole Polytechnique Fédérale de Lausanne (EPFL), Observatoire de Sauverny, 1290 Versoix, Switzerland
[24] Leiden Observatory, Leiden University, Einsteinweg 55, 2333 CC Leiden, The Netherlands
[25] Mullard Space Science Laboratory, University College London, Holmbury St Mary, Dorking, Surrey RH5 6NT, UK
[26] Aurora Technology for European Space Agency (ESA), Camino bajo del Castillo, s/n, Urbanizacion Villafranca del Castillo, Villanueva de la Cañada, 28692 Madrid, Spain
[27] European Space Agency/ESOC, Robert-Bosch-Str. 5, 64293 Darmstadt, Germany
[28] Department of Physics, University of Oxford, Keble Road, Oxford OX1 3RH, UK
[29] Universität Bonn, Argelander-Institut für Astronomie, Auf dem Hügel 71, 53121 Bonn, Germany
[30] Max-Planck-Institut für Astronomie, Königstuhl 17, 69117 Heidelberg, Germany
[31] European Space Agency/ESTEC, Keplerlaan 1, 2201 AZ Noordwijk, The Netherlands
[32] Universität Innsbruck, Institut für Astro- und Teilchenphysik, Technikerstr. 25/8, 6020 Innsbruck, Austria
[33] Department of Physics and Astronomy, University of British Columbia, Vancouver, BC V6T 1Z1, Canada
[34] Dipartimento di Fisica e Astronomia "G. Galilei", Università di Padova, Via Marzolo 8, 35131 Padova, Italy
[35] INFN-Padova, Via Marzolo 8, 35131 Padova, Italy
[36] Ohio University, Physics & Astronomy Department,1 Ohio University, Athens, OH 45701, USA
[37] IFPU, Institute for Fundamental Physics of the Universe, via Beirut 2, 34151 Trieste, Italy
[38] SISSA, International School for Advanced Studies, Via Bonomea 265, 34136 Trieste TS, Italy
[39] Dipartimento di Fisica e Astronomia, Università di Bologna, Via Gobetti 93/2, 40129 Bologna, Italy
[40] INFN-Sezione di Bologna, Viale Berti Pichat 6/2, 40127 Bologna, Italy
[41] INAF-Osservatorio Astronomico di Padova, Via dell'Osservatorio 5, 35122 Padova, Italy
[42] Kapteyn Astronomical Institute, University of Groningen, PO Box 800, 9700 AV Groningen, The Netherlands
[43] ATG Europe BV, Huygensstraat 34, 2201 DK Noordwijk, The Netherlands
[44] Max Planck Institute for Extraterrestrial Physics, Giessenbachstr. 1, 85748 Garching, Germany
[45] Universitäts-Sternwarte München, Fakultät für Physik, Ludwig-Maximilians-Universität München, Scheinerstr. 1, 81679 München, Germany
[46] Institute for Astronomy, University of Edinburgh, Royal Observatory, Blackford Hill, Edinburgh EH9 3HJ, UK
[47] Space Science Data Center, Italian Space Agency, via del Politecnico snc, 00133 Roma, Italy
[48] Dipartimento di Fisica, Università di Genova, Via Dodecaneso 33, 16146, Genova, Italy
[49] INFN-Sezione di Genova, Via Dodecaneso 33, 16146, Genova, Italy
[50] Department of Physics "E. Pancini", University Federico II, Via Cinthia 6, 80126, Napoli, Italy
[51] INAF-Osservatorio Astronomico di Capodimonte, Via Moiariello 16, 80131 Napoli, Italy
[52] European Southern Observatory, Karl-Schwarzschild-Str. 2, 85748 Garching, Germany
[53] Instituto de Astrofísica e Ciências do Espaço, Universidade do Porto, CAUP, Rua das Estrelas, PT4150-762 Porto, Portugal
[54] Faculdade de Ciências da Universidade do Porto, Rua do Campo de Alegre, 4150-007 Porto, Portugal

[55] Dipartimento di Fisica, Università degli Studi di Torino, Via P. Giuria 1, 10125 Torino, Italy
[56] INFN-Sezione di Torino, Via P. Giuria 1, 10125 Torino, Italy
[57] INAF-Osservatorio Astrofisico di Torino, Via Osservatorio 20, 10025 Pino Torinese (TO), Italy
[58] INAF-IASF Milano, Via Alfonso Corti 12, 20133 Milano, Italy
[59] INFN-Sezione di Roma, Piazzale Aldo Moro, 2 - c/o Dipartimento di Fisica, Edificio G. Marconi, 00185 Roma, Italy
[60] Centro de Investigaciones Energéticas, Medioambientales y Tecnológicas (CIEMAT), Avenida Complutense 40, 28040 Madrid, Spain
[61] Port d'Informació Científica, Campus UAB, C. Albareda s/n, 08193 Bellaterra (Barcelona), Spain
[62] Institut d'Estudis Espacials de Catalunya (IEEC), Edifici RDIT, Campus UPC, 08860 Castelldefels, Barcelona, Spain
[63] Institute of Space Sciences (ICE, CSIC), Campus UAB, Carrer de Can Magrans, s/n, 08193 Barcelona, Spain
[64] INFN – Sezione di Napoli, Via Cinthia 6, 80126, Napoli, Italy
[65] Aix-Marseille Université, CNRS, CNES, LAM, Marseille, France
[66] Institute for Astronomy, University of Hawaii, 2680 Woodlawn Drive, Honolulu, HI 96822, USA
[67] Dipartimento di Fisica e Astronomia "Augusto Righi" - Alma Mater Studiorum Università di Bologna, Viale Berti Pichat 6/2, 40127 Bologna, Italy
[68] Jodrell Bank Centre for Astrophysics, Department of Physics and Astronomy, University of Manchester, Oxford Road, Manchester M13 9PL, UK
[69] European Space Agency/ESRIN, Largo Galileo Galilei 1, 00044 Frascati, Roma, Italy
[70] Université Lyon 1, CNRS/IN2P3, IP2I Lyon, Villeurbanne, France
[71] Institut de Ciències del Cosmos (ICCUB), Universitat de Barcelona (IEEC-UB), Martí i Franquès 1, 08028 Barcelona, Spain
[72] Institució Catalana de Recerca i Estudis Avançats (ICREA), Passeig de Lluís Companys 23, 08010 Barcelona, Spain
[73] Institut de Ciencies de l'Espai (IEEC-CSIC), Campus UAB, Carrer de Can Magrans, s/n Cerdanyola del Vallés, 08193 Barcelona, Spain
[74] Université Lyon 1, CNRS/IN2P3, IUF, IP2I Lyon, Villeurbanne, France
[75] Department of Astronomy, University of Geneva, ch. d'Ecogia 16, 1290 Versoix, Switzerland
[76] Université Paris-Saclay, CNRS, Institut d'astrophysique spatiale, 91405, Orsay, France
[77] Institut universitaire de France (IUF), 1 rue Descartes, 75231 PARIS CEDEX 05, France
[78] Aix-Marseille Université, CNRS/IN2P3, CPPM, Marseille, France
[79] INAF-Istituto di Astrofisica e Planetologia Spaziali, via del Fosso del Cavaliere, 100, 00100 Roma, Italy
[80] School of Physics, HH Wills Physics Laboratory, University of Bristol, Tyndall Avenue, Bristol, BS8 1TL, UK
[81] University Observatory, LMU Faculty of Physics, Scheinerstr. 1, 81679 Munich, Germany
[82] Dipartimento di Fisica "Aldo Pontremoli", Università degli Studi di Milano, Via Celoria 16, 20133 Milano, Italy
[83] INFN-Sezione di Milano, Via Celoria 16, 20133 Milano, Italy
[84] Institute of Theoretical Astrophysics, University of Oslo, P.O. Box 1029 Blindern, 0315 Oslo, Norway
[85] California Institute of Technology, 1200 E California Blvd, Pasadena, CA 91125, USA
[86] Caltech/IPAC, 1200 E. California Blvd., Pasadena, CA 91125, USA
[87] Jet Propulsion Laboratory, California Institute of Technology, 4800 Oak Grove Drive, Pasadena, CA, 91109, USA
[88] School of Physics and Astronomy, Lancaster University, Lancaster, LA1 4YB, UK
[89] Felix Hormuth Engineering, Goethestr. 17, 69181 Leimen, Germany
[90] Technical University of Denmark, Elektrovej 327, 2800 Kgs. Lyngby, Denmark
[91] Cosmic Dawn Center (DAWN), Denmark
[92] NASA Goddard Space Flight Center, Greenbelt, MD 20771, USA
[93] Université de Genève, Département de Physique Théorique and Centre for Astroparticle Physics, 24 quai Ernest-Ansermet, CH-1211 Genève 4, Switzerland
[94] Helsinki Institute of Physics, Gustaf Hällströmin katu 2, University of Helsinki, 00014 Helsinki, Finland
[95] Laboratoire d'etude de l'Univers et des phenomenes eXtremes, Observatoire de Paris, Université PSL, Sorbonne Université, CNRS, 92190 Meudon, France
[96] SKAO, Jodrell Bank, Lower Withington, Macclesfield SK11 9FT, UK
[97] Centre de Calcul de l'IN2P3/CNRS, 21 avenue Pierre de Coubertin 69627 Villeurbanne Cedex, France
[98] Dipartimento di Fisica e Astronomia "Augusto Righi" - Alma Mater Studiorum Università di Bologna, via Piero Gobetti 93/2, 40129 Bologna, Italy
[99] Department of Physics, Institute for Computational Cosmology, Durham University, South Road, Durham, DH1 3LE, UK
[100] Institut d'Astrophysique de Paris, UMR 7095, CNRS, and Sorbonne Université, 98 bis boulevard Arago, 75014 Paris, France
[101] Niels Bohr Institute, University of Copenhagen, Jagtvej 128, 2200 Copenhagen, Denmark
[102] Université Paris Cité, CNRS, Astroparticule et Cosmologie, 75013 Paris, France
[103] CNRS-UCB International Research Laboratory, Centre Pierre Binétruy, IRL2007, CPB-IN2P3, Berkeley, USA
[104] Institut de Física d'Altes Energies (IFAE), The Barcelona Institute of Science and Technology, Campus UAB, 08193 Bellaterra (Barcelona), Spain
[105] School of Mathematics and Physics, University of Surrey, Guildford, Surrey, GU2 7XH, UK
[106] Waterloo Centre for Astrophysics, University of Waterloo, Waterloo, Ontario N2L 3G1, Canada
[107] Department of Physics and Astronomy, University of Waterloo, Waterloo, Ontario N2L 3G1, Canada
[108] Perimeter Institute for Theoretical Physics, Waterloo, Ontario N2L 2Y5, Canada
[109] Institute of Space Science, Str. Atomistilor, nr. 409 Măgurele, Ilfov, 077125, Romania
[110] Institute for Particle Physics and Astrophysics, Dept. of Physics, ETH Zurich, Wolfgang-Pauli-Strasse 27, 8093 Zurich, Switzerland
[111] Instituto de Física Teórica UAM-CSIC, Campus de Cantoblanco, 28049 Madrid, Spain
[112] Institut de Recherche en Astrophysique et Planétologie (IRAP), Université de Toulouse, CNRS, UPS, CNES, 14 Av. Edouard Belin, 31400 Toulouse, France
[113] Université St Joseph; Faculty of Sciences, Beirut, Lebanon
[114] Departamento de Física, FCFM, Universidad de Chile, Blanco Encalada 2008, Santiago, Chile
[115] Department of Physics, Royal Holloway, University of London, Surrey TW20 0EX, UK
[116] Infrared Processing and Analysis Center, California Institute of Technology, Pasadena, CA 91125, USA
[117] Cosmic Dawn Center (DAWN)

[118] Universidad Politécnica de Cartagena, Departamento de Electrónica y Tecnología de Computadoras, Plaza del Hospital 1, 30202 Cartagena, Spain
[119] European University of Technology EUt+, European Union
[120] Centre for Information Technology, University of Groningen, P.O. Box 11044, 9700 CA Groningen, The Netherlands
[121] Dipartimento di Fisica e Scienze della Terra, Università degli Studi di Ferrara, Via Giuseppe Saragat 1, 44122 Ferrara, Italy
[122] Istituto Nazionale di Fisica Nucleare, Sezione di Ferrara, Via Giuseppe Saragat 1, 44122 Ferrara, Italy
[123] ICSC - Centro Nazionale di Ricerca in High Performance Computing, Big Data e Quantum Computing, Via Magnanelli 2, Bologna, Italy
[124] Astronomical Observatory of the Autonomous Region of the Aosta Valley (OAVdA), Loc. Lignan 39, I-11020, Nus (Aosta Valley), Italy
[125] Department of Mathematical Physics, Institute of Physics, University of São Paulo, R. do Matão 1371, 05508-090, São Paulo, SP, Brazil
[126] Centre de Recherche Astrophysique de Lyon, UMR5574, CNRS, Université Claude Bernard Lyon 1, ENS de Lyon, 69230, Saint-Genis-Laval, France
[127] Oskar Klein Centre for Cosmoparticle Physics, Department of Physics, Stockholm University, Stockholm, SE-106 91, Sweden
[128] Astrophysics Group, Blackett Laboratory, Imperial College London, London SW7 2AZ, UK
[129] Univ. Grenoble Alpes, CNRS, Grenoble INP, LPSC-IN2P3, 53, Avenue des Martyrs, 38000 Grenoble, France
[130] Dipartimento di Fisica, Sapienza Università di Roma, Piazzale Aldo Moro 2, 00185 Roma, Italy
[131] Institute of Cosmology and Gravitation, University of Portsmouth, Portsmouth PO1 3FX, UK
[132] Institut d'Astrophysique de Paris, 98bis Boulevard Arago, 75014, Paris, France
[133] ICL, Junia, Université Catholique de Lille, LITL, 59000 Lille, France
[134] Center for Astrophysics and Cosmology, University of Nova Gorica, Nova Gorica, Slovenia
[135] MIT Kavli Institute for Astrophysics and Space Research, Massachusetts Institute of Technology, Cambridge, MA 02139, USA
[136] Department of Astronomy, Indiana University, 727 East Third Street, Bloomington, IN 47405, USA
[137] CERCA/ISO, Department of Physics, Case Western Reserve University, 10900 Euclid Avenue, Cleveland, OH 44106, USA
[138] Laboratoire Univers et Théorie, Observatoire de Paris, Université PSL, Université Paris Cité, CNRS, 92190 Meudon, France
[139] Departamento de Física Fundamental. Universidad de Salamanca. Plaza de la Merced s/n. 37008 Salamanca, Spain
[140] IRFU, CEA, Université Paris-Saclay 91191 Gif-sur-Yvette Cedex, France
[141] Universiteit Gent, Department of Physics and Astronomy, Proeftuinstraat 86 N3, 9000 Ghent, Belgium
[142] Konkoly Observatory, HUN-REN CSFK, MTA Centre of Excellence, Budapest, Konkoly Thege Miklós út 15-17. H-1121, Hungary
[143] MTA-CSFK Lendület Large-Scale Structure Research Group, Konkoly-Thege Miklós út 15-17, H-1121 Budapest, Hungary
[144] Université de Strasbourg, CNRS, Observatoire astronomique de Strasbourg, UMR 7550, 67000 Strasbourg, France
[145] Max-Planck-Institut für Physik, Boltzmannstr. 8, 85748 Garching, Germany
[146] Scuola Superiore Meridionale, Via Mezzocannone 4, 80138, Napoli, Italy
[147] Departamento de Física Teórica, Atómica y Óptica, Universidad de Valladolid, 47011 Valladolid, Spain
[148] Laboratory for Disruptive Interdisciplinary Science (LaDIS), Universidad de Valladolid, 47011 Valladolid, Spain
[149] Instituto de Astrofísica e Ciências do Espaço, Faculdade de Ciências, Universidade de Lisboa, Tapada da Ajuda, 1349-018 Lisboa, Portugal
[150] Department of Physics, Astronomy and Mathematics, University of Hertfordshire, College Lane, Hatfield AL10 9AB, UK
[151] Departamento Física Aplicada, Universidad Politécnica de Cartagena, Campus Muralla del Mar, 30202 Cartagena, Murcia, Spain
[152] Instituto de Física de Cantabria, Edificio Juan Jordá, Avenida de los Castros, 39005 Santander, Spain
[153] Observatorio Nacional, Rua General Jose Cristino, 77-Bairro Imperial de Sao Cristovao, Rio de Janeiro, 20921-400, Brazil
[154] Univ. Grenoble Alpes, CNRS, IPAG, 38000 Grenoble, France
[155] CEA Saclay, DFR/IRFU, Service d'Astrophysique, Bat. 709, 91191 Gif-sur-Yvette, France
[156] Dipartimento di Fisica "E. Pancini", Universita degli Studi di Napoli Federico II, Via Cinthia 6, 80126, Napoli, Italy
[157] INFN Sezione di Napoli, Universita degli Studi di Napoli "Federico II", Compl. Univ. di Monte S. Angelo, Edificio G, Via Cinthia, I-80126, Napoli, Italy
[158] Department of Computer Science, Aalto University, PO Box 15400, Espoo, FI-00 076, Finland
[159] School of Physics and Astronomy, University of Nottingham, University Park, Nottingham NG7 2RD, UK
[160] University of Applied Sciences and Arts of Northwestern Switzerland, School of Computer Science, 5210 Windisch, Switzerland
[161] Ruhr University Bochum, Faculty of Physics and Astronomy, Astronomical Institute (AIRUB), German Centre for Cosmological Lensing (GCCL), 44780 Bochum, Germany
[162] DARK, Niels Bohr Institute, University of Copenhagen, Jagtvej 155, 2200 Copenhagen, Denmark
[163] Department of Physics, Centre for Extragalactic Astronomy, Durham University, South Road, Durham, DH1 3LE, UK
[164] Astrophysics Research Centre, University of KwaZulu-Natal, Westville Campus, Durban 4041, South Africa
[165] School of Mathematics, Statistics & Computer Science, University of KwaZulu-Natal, Westville Campus, Durban 4041, South Africa
[166] Department of Physics and Astronomy, Vesilinnantie 5, University of Turku, 20014 Turku, Finland
[167] Finnish Centre for Astronomy with ESO (FINCA), Quantum, Vesilinnantie 5, University of Turku, 20014 Turku, Finland
[168] Serco for European Space Agency (ESA), Camino bajo del Castillo, s/n, Urbanizacion Villafranca del Castillo, Villanueva de la Cañada, 28692 Madrid, Spain
[169] Van Swinderen Institute, University of Groningen, Nijenborgh 3, 9747 AG Groningen, The Netherlands
[170] Department of Physics and Astronomy, University of the Western Cape, Bellville, Cape Town, 7535, South Africa
[171] Department of Physics and Helsinki Institute of Physics, Gustaf Hällströmin katu 2, University of Helsinki, 00014 Helsinki, Finland
[172] Institute for Theoretical Particle Physics and Cosmology (TTK), RWTH Aachen University, 52056 Aachen, Germany
[173] INAF-Osservatorio Astrofisico di Arcetri, Largo E. Fermi 5, 50125, Firenze, Italy
[174] Institute for Theoretical Physics, ETH Zurich, Wolfgang-Pauli-Str. 27, 8093 Zurich, Switzerland
[175] Centro de Astrofísica da Universidade do Porto, Rua das Estrelas, 4150-762 Porto, Portugal
[176] Dipartimento di Fisica, Università di Roma Tor Vergata, Via della Ricerca Scientifica 1, Roma, Italy
[177] INFN, Sezione di Roma 2, Via della Ricerca Scientifica 1, Roma, Italy
[178] HE Space for European Space Agency (ESA), Camino bajo del Castillo, s/n, Urbanizacion Villafranca del Castillo, Villanueva de la Cañada, 28692 Madrid, Spain
[179] STAR Institute, University of Liège, Quartier Agora, Allée du six Août 19c, 4000 Liège, Belgium
[180] Center for Frontier Science, Chiba University, 1-33 Yayoi-cho, Inage-ku, Chiba 263-8522, Japan
[181] Department of Physics, Graduate School of Science, Chiba University, 1-33 Yayoi-Cho, Inage-Ku, Chiba 263-8522, Japan

[182] Dipartimento di Fisica “G. Occhialini", Università degli Studi di Milano Bicocca, Piazza della Scienza 3, 20126 Milano, Italy
[183] School of Physical Sciences, The Open University, Milton Keynes, MK7 6AA, UK
[184] Department of Astrophysics, University of Zurich, Winterthurerstrasse 190, 8057 Zurich, Switzerland
[185] Space physics and astronomy research unit, University of Oulu, Pentti Kaiteran katu 1, FI-90014 Oulu, Finland
[186] Department of Mathematics and Physics, Roma Tre University, Via della Vasca Navale 84, 00146 Rome, Italy
[187] Theoretical astrophysics, Department of Physics and Astronomy, Uppsala University, Box 524, 751 20 Uppsala, Sweden
[188] Minnesota Institute for Astrophysics, University of Minnesota, 116 Church St SE, Minneapolis, MN 55455, USA
[189] Mathematical Institute, University of Leiden, Einsteinweg 55, 2333 CA Leiden, The Netherlands
[190] School of Physics & Astronomy, University of Southampton, Highfield Campus, Southampton SO17 1BJ, UK
[191] Institute of Astronomy, University of Cambridge, Madingley Road, Cambridge CB3 0HA, UK
[192] Department of Physics and Astronomy, University of California, Davis, CA 95616, USA
[193] Kobayashi-Maskawa Institute for the Origin of Particles and the Universe, Nagoya University, Chikusa-ku, Nagoya, 464-8602, Japan
[194] Department of Astrophysical Sciences, Peyton Hall, Princeton University, Princeton, NJ 08544, USA
[195] Fakultät für Physik, Universität Bielefeld, Postfach 100131, 33501 Bielefeld, Germany
[196] Department of Physics and Astronomy, Lehman College of the CUNY, Bronx, NY 10468, USA
[197] American Museum of Natural History, Department of Astrophysics, New York, NY 10024, USA
[198] SRON Netherlands Institute for Space Research, Landleven 12, 9747 AD, Groningen, The Netherlands

⋆ e-mail: iatereno@ciencias.ulisboa.pt

Appendix A: Exposure maps

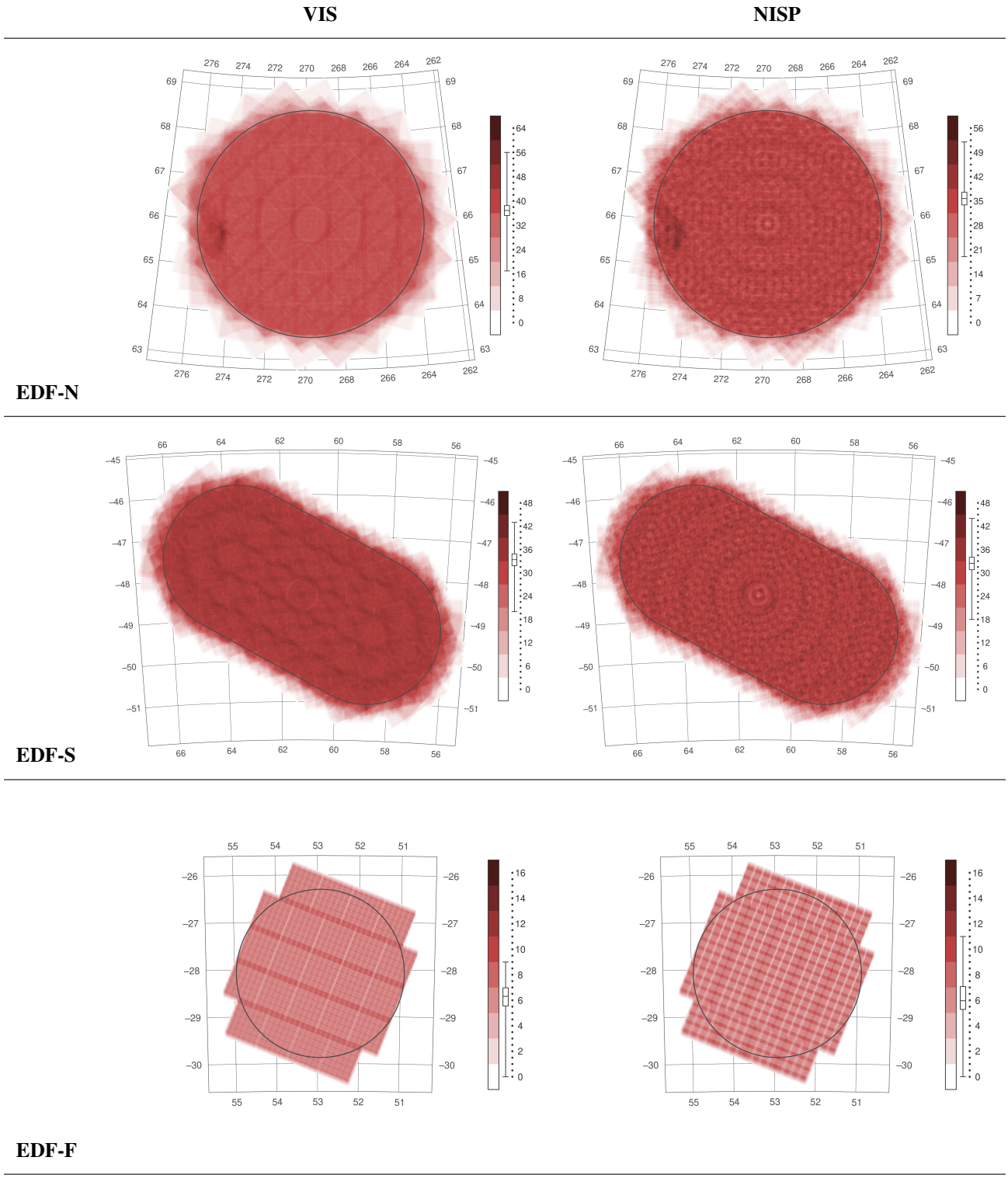


Fig. A.1. DR1 exposure maps of the Euclid Deep Fields per instrument. The depth is given by the number of single dither exposures per pixel. The scale includes a quartile bar, with the lower tick showing the first quartile (the median of the lower half of the exposure values), the middle tick showing the second quartile (the median of the full set of values), and the upper tick showing the third quartile (the median of the upper half of the exposure values). The box within the bar shows the inter-quartile range, i.e., the spread of the middle half of the points.

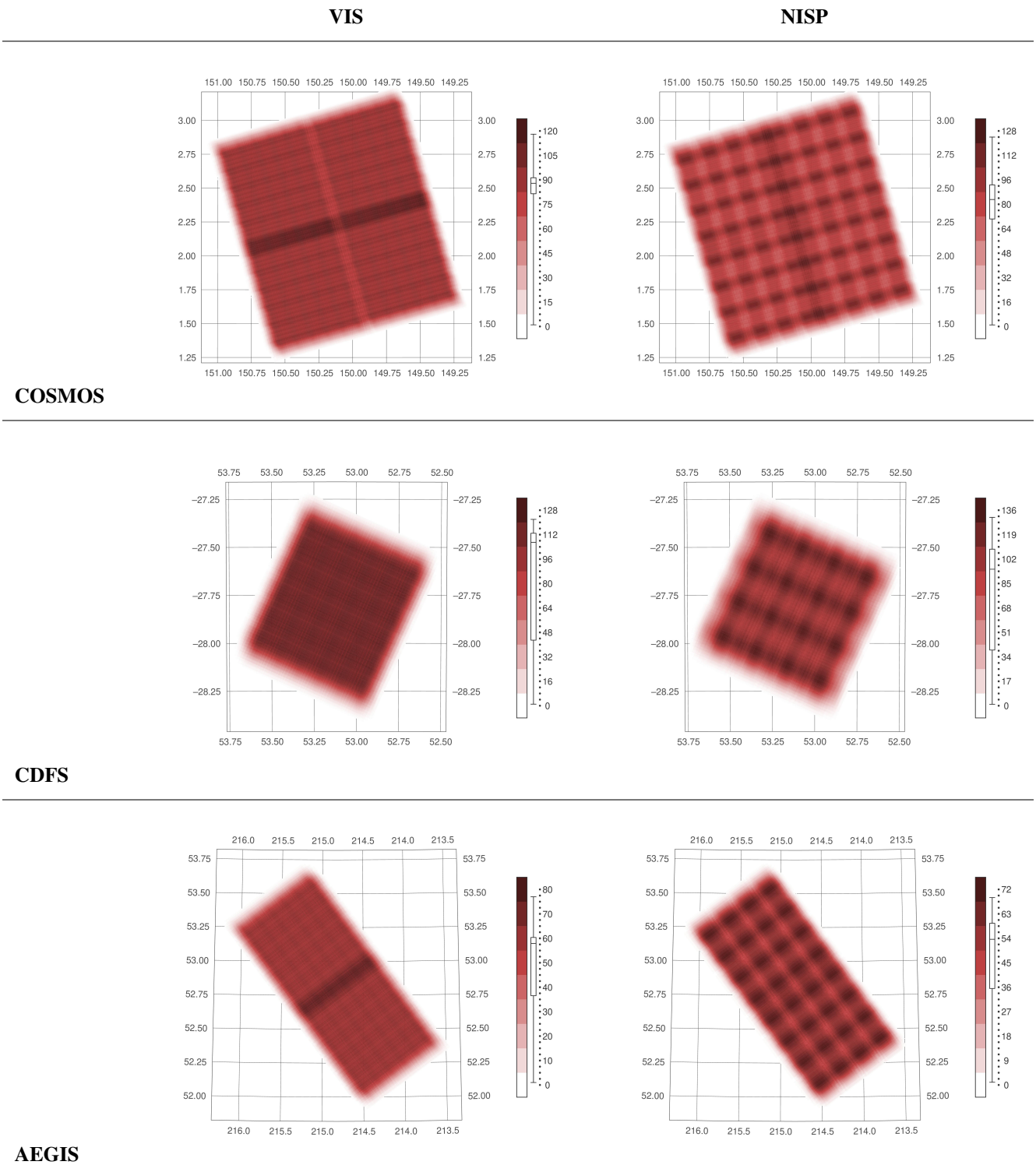


Fig. A.2. Same as Fig. A.1 but for the Euclid Auxiliary Fields.

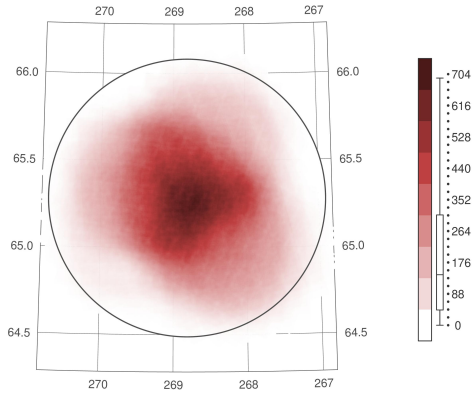
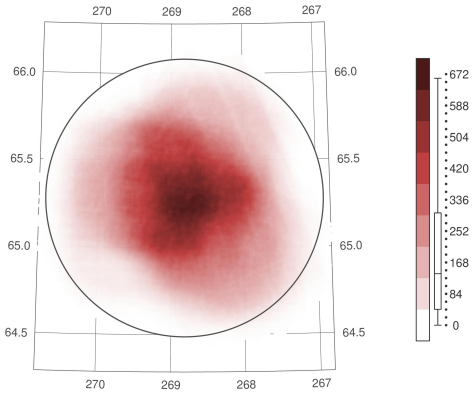
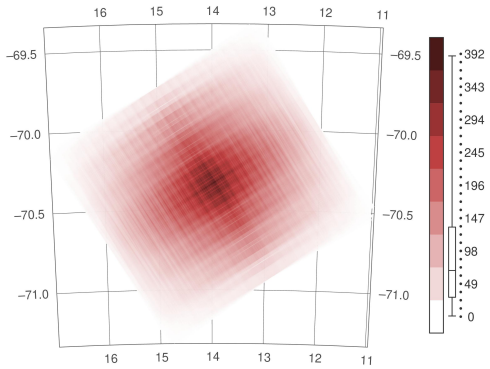
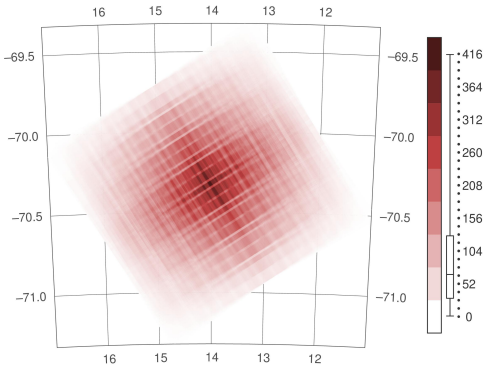
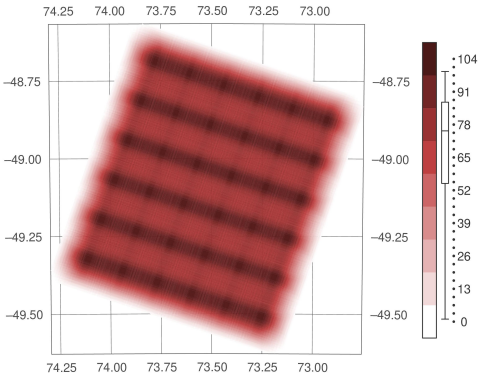
	VIS	NISP
Self-calibration		
PN		
PSF		

Fig. A.3. Same as Fig. A.1 but for the calibration fields.

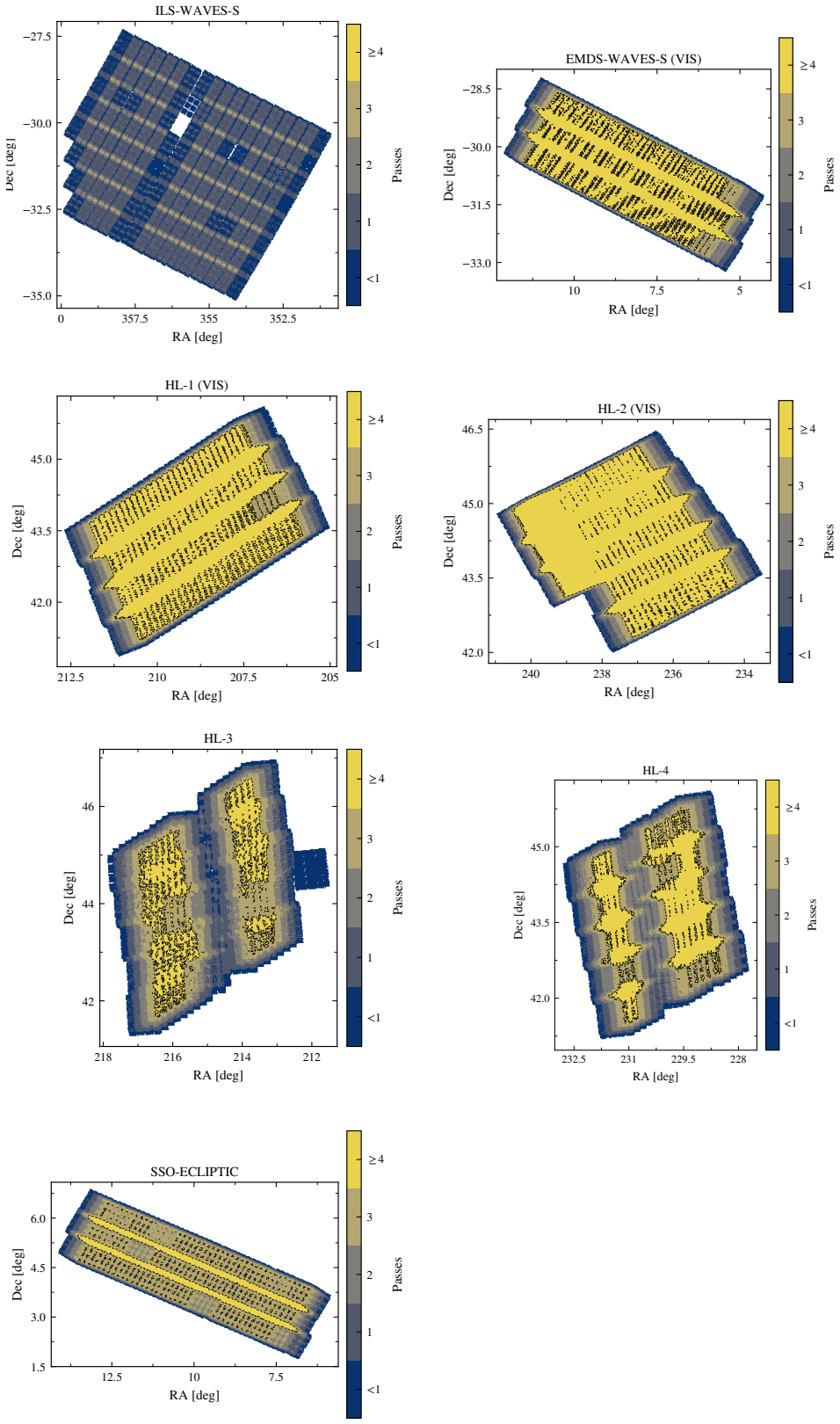


Fig. A.4. DR1 exposure maps of the PDC science fields. The depth in each pixel is given by the minimum number of 4-dither exposures between the VIS and NISP counts (for fields observed with ROS), or by the number of 4-dither VIS exposures (for fields only observed with VIS).

Appendix B: Acronyms and Glossary

Table B.1. List of acronyms used in this paper with a glossary of terms.

Acronym	Definition	Glossary
AA	α angle	*Euclid*'s roll angle
AEGIS	AEGIS strip	EAF for colour gradient calibration
BGS	Blue grism	The shortest wavelength grism in NISP
CalF	Calibration Framework	The repository of calibration specifications
CCB	Configuration Control Board	A group that approves changes to a system
CDFS	Chandra Deep Field South	EAF for photometric redshift calibration, within EDF-F
COSMOS	Cosmos Evolution Survey	EAF for photo-z and colour gradient calibrations, at the edge of the RoI
CPC	Completeness and Purity calibration	Visits to EDFs with different orientations to decontaminate the spectra
DES	Dark Energy Survey	Provides ground-based data in the southern sky
DR1	Data Release 1	The first large Euclid DR, including roughly 2000 $\deg^2$ of EWS
EAF	Euclid Auxiliary Field	Well-known fields that *Euclid* visits multiple times
EC	Euclid Consortium	Instruments building, scientific data processing, and exploitation
EDF-F	Euclid Deep Field Fornax	The smallest field of the EDS
EDF-N	Euclid Deep Field North	The most accessible field of the EDS, in the NEP
EDF-S	Euclid Deep Field South	The largest field of the EDS
EDS	Euclid Deep Survey	The deep tier of the *Euclid* surveys
EES	Euclid Ecliptic Survey	Survey of Solar System objects made in PDC thermalisation time
EGBS	Euclid Galactic Bulge Survey	A survey made expressly for Q2
EMDS	Euclid Medium-Deep Survey	Tentative intermediate depth tier made in PDC thermalisation time
ERO	Early Release Observations	The very first *Euclid* data release
ESS	Euclid Survey System	SOC mission planning subsystem
ESSOT	ESS operational tool	ESS tool that generates an OSS from an RSD and also generates SSRs
EST	Euclid Science Team	Team supporting the project scientist in maximising the scientific return
EUDF	Euclid Ultra-Deep Field	The deepest *Euclid* field in preparation
EWS	Euclid Wide Survey	The main component of the Euclid survey
FGS	Fine-Guidance Sensor	A dedicated instrument to find guide stars
FWA	Filter-wheel assembly	Rotating device that holds multiple filters
GWA	Grism-wheel assembly	Rotating device that holds multiple grisms
ICR	Instrument Commanding Request	IOT input to specify low-level instrument commands on the OSS
ILS	Independent Legacy Scientist	Two scientists external to the EC with selected rights to *Euclid* data
IOT	Instrument Operation Team	Two EC teams for operational support and monitoring of the instruments
LE1	Level 1	Raw uncalibrated data, processed by SOC from raw spacecraft telemetry
LE2	Level 2	Calibrated and co-added images and spectra, processed by EC SGS PFs
MOC	Mission Operations Centre	ESA, executes the operations and controls the spacecraft
NEP	North ecliptic pole	Always visible to *Euclid*, location of the EUDF
NISP	NIR Spectrometer and Photometer	Instrument, near-infrared wide-field imager and spectrometer
OSS	Operational Sky Survey	Operational survey generated with ESSOT from an RSD and ICRs
PC	Planning cycle	The interval between two SOPS windows, duration of an SSR
PDC	Phase-diversity calibration	In-flight calibration campaign for the wavefront model of the telescope
PF	Processing Function	Specialized EC SGS data processing pipelines
POR	Payload Operations Request	Low-level operational product generated with SCS from OSS for MOC
PV	Performance-Verification	Early operations phase for in-flight characterisation of the instruments
Q1	Quick Data Release 1	DR not suited for cosmology with data from 1 pass on each EDF
Q2	Quick Data Release 2	DR not suited for cosmology with data from the EGBS
RGS	Red grism	The two longest wavelength grisms operating in NISP
RoI	Region of Interest	The extragalactic sky where the EWS is built
ROS	Reference Observing Sequence	Observing sequence used in EWS, EDS, and EAFs observations
RSD	Reference Survey Definition	Schedule of pointings and slews for science operations made by SOST
SAA	Solar aspect angle	*Euclid*'s pitch angle
SCS	SOC Commanding System	SOC subsystem that generates telecommands for a planning cycle
SGS	Science Ground Segment (EC)	Produces the science-ready calibrated images and source catalogues
SOC	Science Operations Centre	ESA, mission planning, monitoring, LE1 processing, and archive
SOPS	Special Operations	Periodic time window allocated spacecraft and orbit mainenance
SOST	Survey Operations Support Team	The survey scientist's EC team that produces the RSDs for SOC
SSR	Survey Schedule Request	High-level product generated from an OSS with ESSOT for MOC
UNIONS	UV NIR Optical Northern Survey	Provides ground-based data in the northern sky, from three observatories
VIS	Visible instrument	Instrument, wide-field optical imager